TUDelft
Delft University of Technology

Challenge the future

Contents

1 Abstract

Life at low-Reynolds numbers regime is intriguing [1]. Single motile bacteria are known to exhibit erratic behaviour; they swim in what is known as a random walk, alternating between periods of swimming straight and abrupt moments of re-orientation [2]. Yet in dense populations, cells of *E.coli* have been reported to exhibit weak synchronization and self-organize into collective oscillatory motion patterns [3]. However, the origin of this rhythmic behaviour remains largely unknown. Here, we present a method of inducing self-sustained oscillations over minute timescales in single *E.coli* cells by trapping them in circular microcavities. By engineering the size of these microwells, we show that the velocity of single *E.coli* can be tuned between speeds ranging from a few to $20\mu m/s$. Furthermore, we show that by connecting the microwells via on-chip channels, *E.coli* tend to coordinate their motion through hydrodynamic interaction and exhibit collective dynamics. Using analytical modeling, we extract the coupling strength and design the channels to mediate synchronized oscillation between two bacterial oscillators. Our work not only advances our understanding of the collective dynamics of swarming bacteria but also provides the first evidence for single-cell bacterial oscillators, paving the way to using micro-organism-inspired oscillations in applications as varied as antibiotic screening [4], scientific computing [5] and micro-swimmers [6].

2 Introduction

Motility is a crucial driver for bacterial prosperity [7] and enables cells to move around and exploit their environment to find nutrients, avoid toxins, and locate favorable habitats [8]. Bacterial motility has intrigued scientists for decades, and is not only of fundamental interest but provides insights into the formation of biofilms [9], propagation of infections [10] and is an important factor in the development of bacterial resistance to antibiotics [11]. *Escherichia coli* (*E.coli*) is widely regarded to be a model organism for bacterial research on flagellum-driven swimming [12], which, in the absence of external stimuli, employs a swimming strategy that closely resembles a random walk. It has been shown however that when swimming close to surfaces, *E.coli* suppress their re-orientation frequency and are instead guided by their physical boundaries [13]. This has opened an entirely new field of research based on the concept that the control of bacterial motion lies in the design of physical boundaries. Bacterial swimming and ordering have been studied in a wide range of confinements, from lattices of interconnected microwells [14] to microfluidic circuits resembling racetracks [15]. Dense bacterial populations have been reported to transition into distinct collective motion patterns upon setting the proper confinement configuration. However, the underlying drivers for coupled motion remain unresolved.

Oscillations and synchronization have a pivotal role in living organisms [16]. Over several thousands of years of mammalian evolution, processes such as the synchronous beating of pacemaker cells in the heart [17] and the synchronized firing of neuron networks in the brain [18] have remained ubiquitous across species. Even organisms as small as *C. reinhardtii* algae, which measure approx. 10 μm in diameter, have been seen to exhibit synchrony in their flagellar stroke [19]. However, the exact mechanism behind this process is, in many cases, not obvious. Here, we further simplify the system of biological oscillators to just single cells of *E.coli* (0.8 μm in diameter, 2–4 μm in length). While *E.coli* in dense populations have been shown to display large-scale collective oscillations [3], there are no previous demonstrations of synchronized oscillations at the single cell level. To this end, we design on-chip circular microcavities suitable to trap and isolate single cells of *E.coli* from a suspension. The trapped cells swim predominantly along the cavity wall, and as such, the cell motion is shaped by the boundary to result in neatly periodic rotations. Our results show that this periodic motion of cells can sustain over several minutes and slow down in more confining cavities, suggesting cell motion to be tuneable. Furthermore, by connecting cavities via microchannels, the *E.coli* are coupled through hydrodynamic interaction and exhibit various types of collective dynamics, such as slow-fast coupled motion, in-phase synchronization with periodic kicks, and switching between in-phase and anti-phase synchronized states. These coupled motions of cells are demonstrated to agree with the simple Adler model, which is used to extract the coupling strength. In this way, we engineer microchannels to mediate coupling between just two *E.coli* cells, showing synchronization to be a phenomenon present in even the simplest active matter systems.

3 Problem definition

Living cells are highly sensitive to the mechanical properties of their surrounding environment. Research conducted over the past few decades has revealed that, besides chemotaxis, physical factors such as stiffness, hydrodynamic forces, and geometry strongly influence cell structure and cellular decision making [20]. There exist a wide range of mechanical characterisation techniques that are currently used to determine the role of mechanical forces in cell biology [21]. Highly sensitive cell characterisation tools, such as optical tweezers [22] and atomic force microscopy (AFM) [23] have become popular methods for single molecule force spectroscopy. Besides, the wide availability of microelectromechanical systems (MEMS) since the 1990's [24] has provided researchers new platforms to experimentally study the behaviour of cells in controlled micro-environments. Single-cell-confinement methods such as the microwell arrays proposed by Rettig, J. et al. (2005) [25], and the microfluidic trapping assays by Pitruzzello, G. et al. (2019) [26] have been shown crucial for the rapid analysis of microbes with high-throughput. Nonetheless, they have the inherent limitation that pinned-down microbes behave differently than motile microbes in tissue, as the constraint on motility may in principle affect cell function. The first research goal for this thesis is therefore stated to be the following:

The first research objective is to find a method to trap single cells of *E.coli*, which allows for the monitoring of localized motion of a large number of cells simultaneously.

Bacteria have adopted various means to propel themselves [27]. While the variety of bacterial swimming mechanisms is diverse, they abide by the same rule that motion at the micrometer scale is governed by viscous damping [28]. Thus, swimming strategies employed by microorganisms that operate at low Reynolds numbers have evolved to overcome and exploit viscous drag forces. *E.coli* is widely regarded to be a model organism for bacterial research on flagellum driven swimming. They are embedded with long (5-10μm) flagellar filaments, which when rotated in clockwise manner, bundle behind the cell body and create thrust in aqueous media [12]. In the bulk of the culture, unimpeded by any surface or obstacle, *E.coli* alternate periods of straight swimming, called 'runs', with moments in which they re-orientate, referred to as 'tumbling'. By increasing or decreasing the tumbling frequency, a behavioural process called 'chemotaxis', cells are able to migrate towards chemical attractants, or move away from certain chemical repellors inside their environment. It has been shown however that near flat surfaces, cells suppress their tumbling frequency by up to 50% [13], indicating that swimming cells can be trapped close to surfaces. Surprisingly, in the vicinity of surfaces *E.coli* digress from swimming straight, and are instead seen to swim in clockwise circular trajectories [29]. A transition that is owed to the characteristic swimming mechanic of *E.coli*, which near surfaces produces viscous forces that act perpendicular to their direction of motion [30]. In more restricted geometries, such as narrow rectangular microchannels with width smaller than, or comparable to the length of flagella, cells have been observed to undergo a transition to unidirectional swimming [31], and exhibit a preference to swim at the right-hand side [32]. However, while this ordering of cells to the right proposedly originates from the inherent clockwise circling of *E.coli* near flat surfaces, the general wall-following characteristic of *E.coli* has been suggested to derive largely from hydrodynamic surface entrapment [33]. This emergent cell-surface interaction enables *E.coli* to follow convex walls [34], be guided to steer through funnels [35] and notably drive micro-

mechanisms [36], just highlighting the potential of directed cell motion.

Bacterial motion (in absence of any chemical gradients) has been studied in a wide range of confinements [37], and has led to the broad consensus that confined cell motion is governed by hydrodynamics and steric interactions with surfaces, either leading to the smooth navigation of cells through microchannels, or to trapping. Specific designed geometries may however provide a compromise, e.g. circular microwells have been found to both trap *E.coli* and guide their motion into contained vortices [38]. Interestingly, in microwell doublets these vortices have been shown pairable an may align or oppose depending on the center distance between wells [39]. In addition to the study of bacterial motion in microwell doublets, studies exploring geometries such as microwell lattices [14] and oval shaped tracks [15] lay a strong foundation for the argument that the key to controlling collective order lies in setting the geometric configuration. As such, assuming single cells can be trapped in a way they remain motile, the next objective is stated to be the following:

The second research objective is to, by means of tuning the geometric configuration of traps, control the motility of trapped *E.coli* cells.

In the introduction it was stated that there is a growing interest towards the topic of synchronization, a complex phenomenon which seems to suggest invisible attraction between interacting rhythms. To better understand what mechanics exactly contribute to self-organization in biology, empirical studies have primarily focused on populations of microorganisms. Liu J. et al. (2015) [40] observed that within microbial biofilm communities, nutrient starvation drives collective growth rate oscillations. In other work it has been shown that in dense bacterial populations, local interactions give rise to large-scale collective motion, explaining cell motility to be the deciding driving factor [3]. Research on collective bacterial motion has primarily focused on populations of cells, which are complex systems subject to many potential types of interaction mechanisms. Individual swimmers can physically collide, create hydrodynamic forces felt by others, possibly transfer chemical cues, etc. In order to achieve better understanding in the intricacies of bacterial self-organization, it is thus necessary to simplify the system of biological oscillators. The last research goal for this thesis is therefore stated to be the following:

The final research objective is to asses whether *E.coli* at the single cell level, trapped and without physical contact, show coupled oscillatory motion

To this extent a geometric configuration is designed which is is able isolate and trap single bacterial cells from the bulk. Next, trapping sites are connected such that cells remain physically separated, but are interacting through hydrodynamic flow. In this way there is a potential to gain more insight in the role of hydrodynamics in ordered collective motion.

4 Single cell bacterial oscillators

4.1 Single bacterium oscillators

The experiments were performed with (smooth sailing) *E.coli* CheA in LB medium, grown following the method outlined in Methods 6.3, that were dispensed on patterned poly-dimethyl siloxane (PDMS) samples (see Methods 6.1.3). The PDMS samples were equipped with arrays of open microcavities that measure $2.5\mu m$ in depth with diameters ranging from $5\text{-}30\mu m$ (see Methods 6.2.2). Suspended *E.coli* were found to settle inside cavities and stay trapped for up to 13 minutes (see Extended data 8.1). Interestingly, in inverted cavities cells were able to overcome gravity and swim at the ceiling, indicating surface entrapment to be the driving factor behind cell trapping (see Supplementary 8.7). We recorded the motion of cells inside microcavities using a microscopic setup as depicted in figure 1a, and found cells to swim systematically in clockwise direction along the cavity wall, which was readily expected from the right-handedness of *E.coli* [32]. Microscopic recordings were post-processed via a custom tracking algorithm, elaborated upon in Methods 6.4.1, which tracked the position of the cell center relative to that of the cavity. Figure 1c-d presents such an example, where an *E.coli* cell was swimming inside an $8\mu m$ microcavity, and the tracking software retrieved the cell position over time. We observed cells in circular cavities to swim smoothly with fairly constant speed, see the bottom panel of figure 1d. Note that the measured high frequency noise around the mean baseline originated from imperfections in the cell detection algorithm. It is also noteworthy that over the trapping duration, cell tumbling events almost completely disappeared, and when they did sporadically occur, it was often the method by which trapped *E.coli* escaped.

Trapped inside circular microcavities, *E.coli* have shown to transform their inherent random-like motion [2] into ordered limit cycle oscillations. To clarify the role of confinement on cell motility, we compared the motion of trapped *E.coli* in different sized microcavities (fig 2). Figure 2a shows two examples of measured cell trajectories for a $7\mu m$ (left panel) and $25\mu m$ (right panel) microcavity respectively. Whereas cells trapped in confining microcavities (cavities smaller than the size of *E.coli* including flagella) have been found to principally follow the cavity wall, in large cavities (more than twice the size of *E.coli* including flagella) cells exhibited two distinct states of swimming (see Supplementary 8.2). In $25\mu m$ cavities, trapped cells were observed to alternate periods of clockwise spiraling in the cavity interior, with periods of swimming clockwise along the cavity wall, suggesting cells to both show typical free surface motility behaviour [30], see also Supplementary 8.3, as uni-directional wall-following [31]. Figure 2b shows averaged bacterial activity heat maps for both $7\mu m$ and $25\mu m$ cavities, generated from superimposed cell trajectories measured in identical cavities respectively. From superposition of 271 cell trajectories we found bacterial activity in $7\mu m$ cavities for 99% to be concentrated in the area $2\mu m$ from the cavity edge, whereas in $25\mu m$ cavities this reduced to 77%, measured over 92 trajectories (see Methods 6.4.4). The heat maps confirm that bacterial activity, besides being largely concentrated in the outer ring in both cases, in large cavities as well spread towards the cavity interior. We deduce from the two-state dynamic behaviour of cells that the driving factor for wall-following stemmed from hydrodynamic surface entrapment [33] of cells near the cavity wall, rather than the preferential turning of cells near flat surfaces.

To further characterize the tunability of cell motility, we measured cell motion in a range of confinement sizes (fig 2c), following the method of data analysis outlined in Methods 6.4.2-6.4.3. Results show that cells slowed down significantly when confined, reducing in speed from $10\mu m/s$ in cavities with diameter $d \geq 14\mu m$ to $5\mu m/s$ for $d \leq 6\mu m$ approximately. Furthermore, we note that from $d = 14\text{-}30\mu m$ cell speed plateaued, assymptoting towards 75% of the measured cell free surface speed. The drop-off in cell speed initiates approximately at the point cavities were shrunk below the size an *E.coli* cell including flagella. We speculate that below this size, the confining boundaries of cavities either forced increased curvature of the flagellar bundle, or to have forced the bundle (partly) outside of the cavity, both scenarios leading to increased outward-radial or out-of-plane forces and thus enhanced surface drag. Results suggest the swimming speed of trapped cells to be highly sensitive to the cavity diameter. Nonetheless, we observed similar cell residence times over the range of trap sizes (fig 2d), defining residence time as the duration an *E.coli* cell is swimming along the cavity wall uninterruptedly. On average, microcavities were able to sustain limit cycle oscillations of *E.coli* for approximately $1min$, regardless of cavity size, considering measurements that lasted $2min$ each.

4.2   Coupled bacterial oscillators

By means of trapping *E.coli* in circular microcavities, we observed inherently chaotic bacterial motion [2] to order into neat tunable limit cycle oscillations. Furthermore, to capture the coupling dynamics between just two cells, we extracted the phase positions $\varphi_{1,2}$ (see fig 3a) from videos of adjacent trapped cells. The time-dependent normalized phase difference $cos(\varphi_1 - \varphi_2)$ was used to characterize the relation between the cyclic motion of two cells. Examining the phase difference dynamics of cells in adjacent $5-8\mu m$ sized microcavities distanced $4\mu m$ apart, we found cells to behave as rotators with constant intrinsic frequencies $\dot{\varphi}_{1,2} = \omega_{1,2}$, so that $cos(\varphi_1 - \varphi_2) = cos(\psi t)$, with $\psi = \omega_1 - \omega_2$ (see Supplementary fig 18b).

Observations from the behaviour of active systems in microfluidic experiments have lead to the broad consensus that long-range hydrodynamic interactions are able to drive synchronization [41]. As such, motivated by previous experimental observations [14][39], we designed sets of microcavities that are connected via on-chip channels (see fig 3b). In this configuration, cells no longer strictly behaved as independent rotators, thus $\dot{\varphi}_{1,2} \neq \omega_{1,2}$, but were instead observed to exhibit coupled behaviour, including periodic slow-fast dynamics, as shown in supplementary figure 18d. To capture the coupling dynamics we formulate an Adler model [42] (see Supplementary section 7.2.1), describing the phase difference $\phi = \varphi_1 - \varphi_2$ to evolve according to a first-order differential equation of the form: $\dot{\phi} = f(\phi)$ (eq 1)

$$\dot{\phi} = \Delta\omega - ksin(\phi - \phi_0) \tag{1}$$

Here $\Delta\omega$ represents the frequency mismatch $\omega_1 - \omega_2$ between cells, k the coupling strength and ϕ_0 the phase delay of the hypothetical restoring force. Noteworthy is that phase-locking between cells ($\dot{\phi} = 0$) can only exist as a stable state for $\lim\limits_{t\to\infty}(f(\phi))$, when the frequency mismatch is small enough relative to the coupling strength, or $|\Delta\omega| \leq k$ [43]. However, the periodic slow (in-phase) - fast (out of phase) dynamic behaviour of $cos(\varphi_1 - \varphi_2)$ that is observed more resembles the case where $|\Delta\omega| > k$, and $\phi_0 = -\pi/2$ (see supplementary

fig 20). By means of parameter estimation (Supplementary sec 7.2.2) we fit the measured phase difference data with the Adler model, see figure 3c-d, and as such extract the coupling strength. We find the channel geometry to mediate coupling between cells, and observed increased coupling in short (fig 3e) and wide (fig 3f) channels. Note that the considered range of channel configurations was limited due to the potential of PDMS collapse in narrower/shorter channels, and the increased potential of *E.coli* to swim through upon further widening them.

4.3   Controlled synchronization of bacterial cells

In order to achieve synchronization between cells, we extracted the coupling strength through modelling the phase difference dynamics as slow-fast coupling ($|\Delta\omega| > k$), helping us to engineer channels to mediate coupling. Results show that cells alternate periods of oscillating in synchrony with phase-slips, showing 2π periodic evolution of the phase difference (see fig 4a). However, while the slow-fast Adler regime adequately describes most experimental observations (see Supplementary section 8.4), we found different types of dynamics to appear between cells.

In addition to slow-fast dynamics, cells were seen to express slow dynamics both in-phase and in anti-phase, interrupted by fast phase-slips (as shown in figure 4b). Instead of expanding the Adler model to include additional slow dynamics in anti-phase, we suggest the phase difference behaviour may be modelled assuming cells sustained both in-phase as well as anti-phase synchronization, alternated by fast phase-slips. Furthermore, we note the clear periodicity in phase-slips to suggest a source of periodic perturbations. It is evidenced by video recordings that on-chip microchannels in many cases indeed functioned as obstruction, and cells have been seen to cyclically collide into the channel opening upon traversing the cavity, causing them to stop moving momentarily. Perturbation events which had enough impact to always force a phase-slip led to instances of highly periodic switching between in-phase and anti-phase synchronization (see Supplementary figure 28). Nonetheless, measurements of cells which were observed to display variance in phase-slip frequency (see Supplementary figure 29) imply perturbations can be more adequately described as periodic impulses with random amplitude. This type of coupling is not captured well by the proposed Adler function (eq 6), but instead may be interpreted as an over-damped particle in a tilted washboard potential (see fig 4b right panel). As such, phase-slips occurred at times when the periodic impulse was strong enough kick the system out of equilibrium.

A third type of coupling is presented in figure 4c, where cells have been found able to retain their synchronized state upon accumulation of a phase offset, thereby resisting a full phase-slip. This dynamic implies in-phase synchronization was a stable equilibrium state, which may be modelled by the proposed Adler equation in the regime where $k > |\Delta\omega|$ (see Supplementary sec 8.6.2).
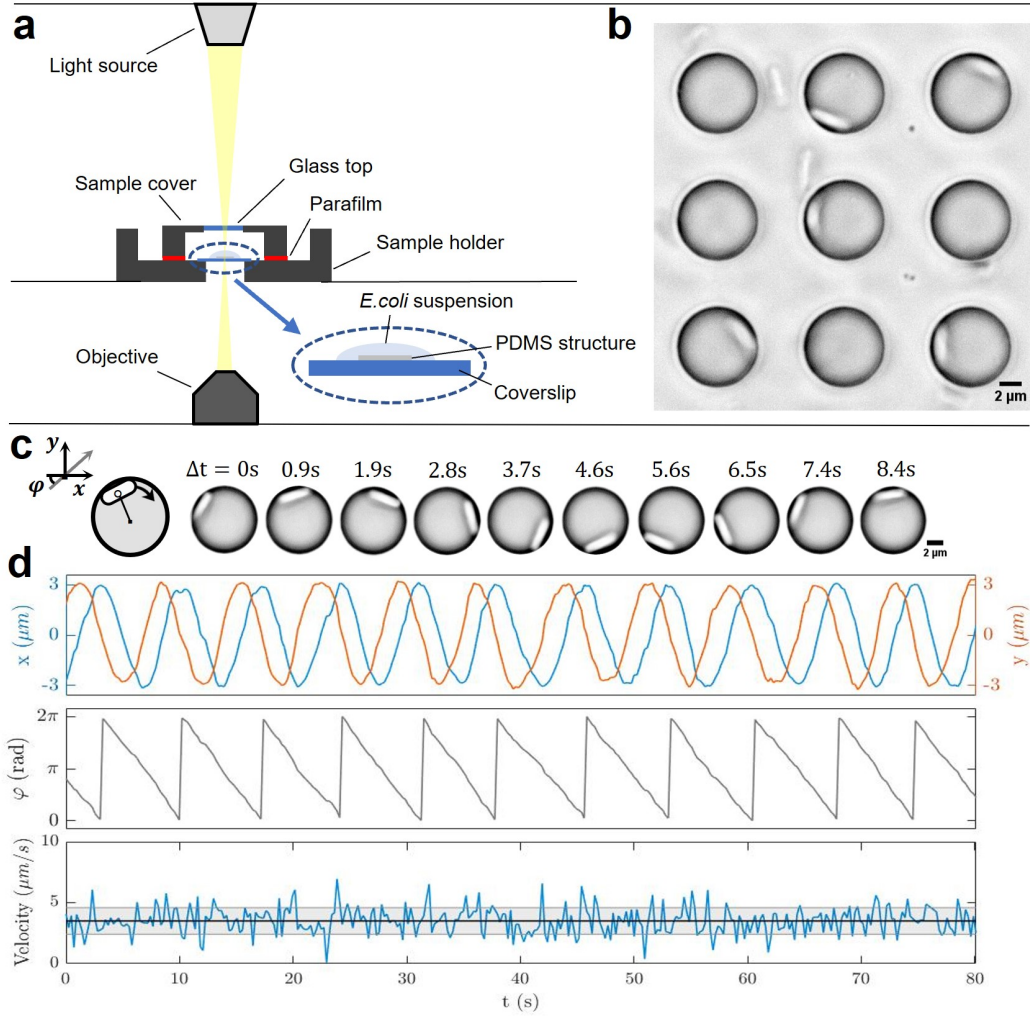
Figure 1: Experimental method for measuring cell motility in confinement. (a) Schematic of microscope setup. (b) Microscopic image of *E.coli* cells trapped in microcavities. (c) Motion of a cell inside a microcavity ($8\mu m$ diameter). On the left we present a schematic of considered coordinate system, the position of the cell center is measured relative to that of the cavity. Right of the schematic we show a sequence of cell positions as captured by microscope with added relative time stamps. (d) Three diagrams displaying cell tracking data. The top diagram shows tracked x (in blue) and y (in orange) coordinates. The middle diagram indicates cell phase angle. The diagram on the bottom shows tangential velocity between sequential frames (in blue), with a black line indicting mean speed and grey shadow corresponding to the standard deviation.
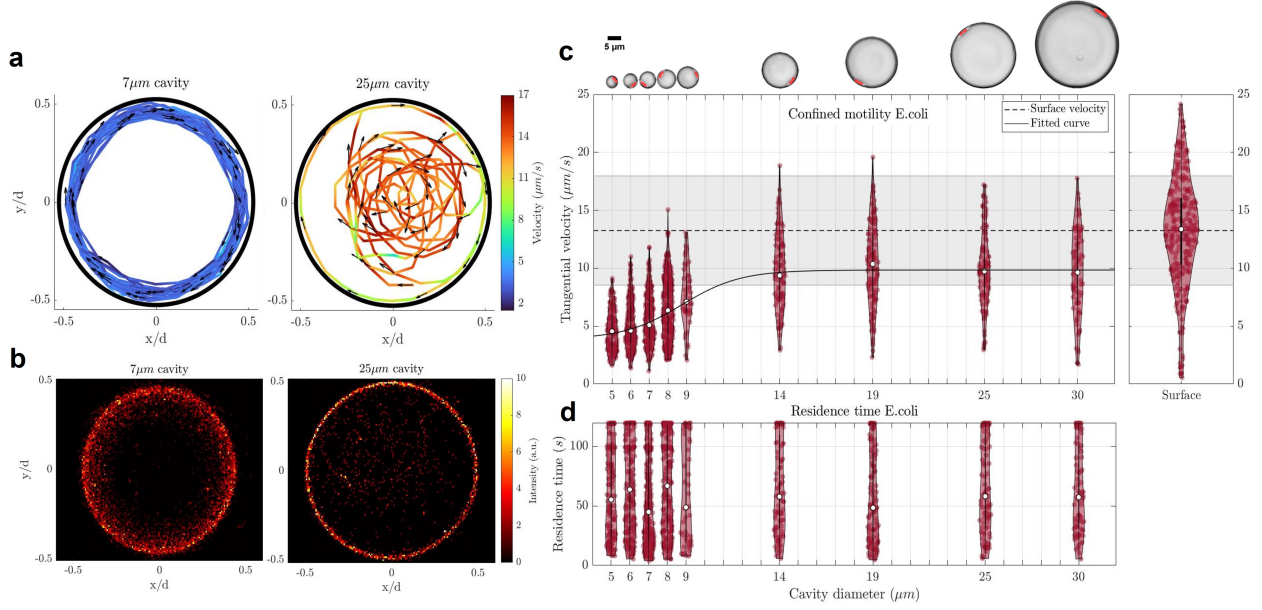
Figure 2: Motility behaviour of confined *E.coli*. (a) Two measured cell trajectories in a $7\mu m$ (left panel) and $25\mu m$ (right panel) cavity. Trajectories are colored corresponding to a velocity scale displayed in the right color bar, arrows indicate swimming direction. (b) Averaged heat maps indicating the distribution of bacterial activity in $7\mu m$ (left panel) and $25\mu m$ (right panel) cavities. (c) Velocity distributions of trapped *E.coli*, displayed as violins, as a function of cavity diameter. The data (medians) is fit with a smooth s-curve shown with a black line. The right panel corresponds to the violin distribution of cell swimming speed over a free surface, the mean is highlighted in the background by a dotted line equipped with a grey shade indicating standard deviation. (d) Residence times of trapped *E.coli* as a function of cavity diameter. Recordings were cut-off at the $2min$ mark.
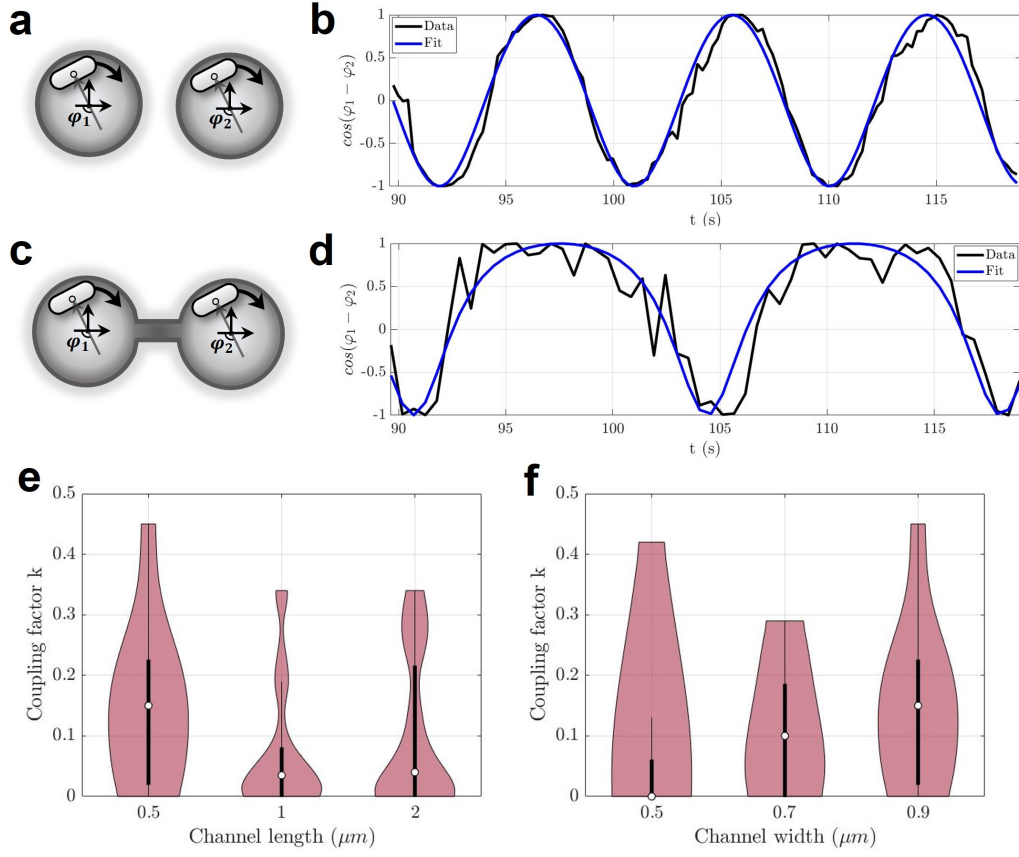
10

Figure 3: Effect of channels on coupling dynamics between pairs of cells. (a) Schematic of cells in uncoupled cavities. (b) Measured phase difference of two cells in uncoupled cavities (in black), fitted with the Adler model (in blue). (c) Schematic of cells in coupled cavities. (d) Measured phase difference of two cells in coupled cavities (in black), fitted with the Adler model (in blue). (e) Coupling strength distribution for different channel lengths of connected cavities measuring $7\mu m$ in diameter. Channel widths are fixed at $0.9\mu m$ for each of the distributions. (f) Coupling strength distribution for different channel widths of connected cavities measuring $7\mu m$ in diameter. Channel lengths are fixed at $0.5\mu m$ for each of the distributions.
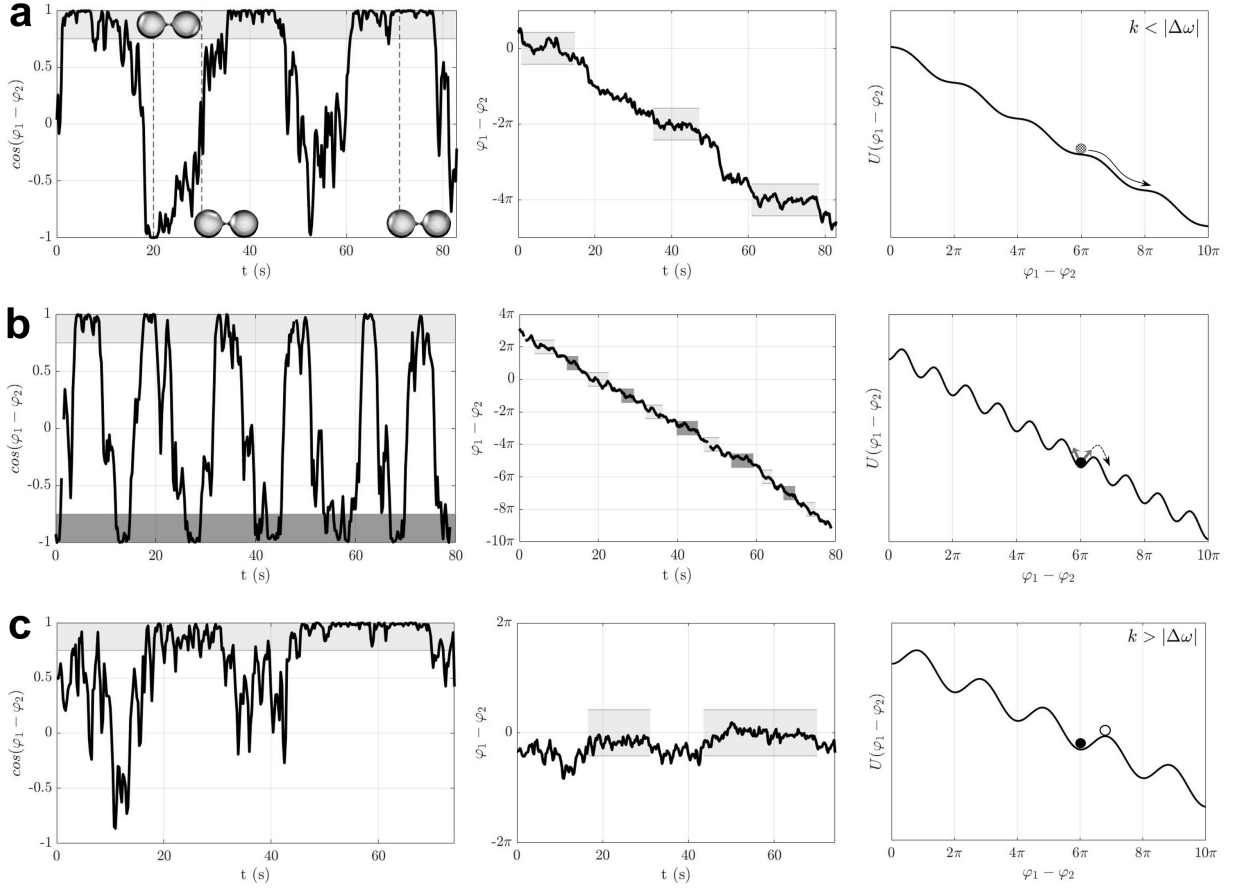
Figure 4: Three types of coupled dynamics measured between cells in connected microcavities. Left and middle panels respectively show the wrapped and unwrapped phase difference data between two cells, functioning as examples for each of the observed dynamics. Grey shades highlight the periods cells were observed to be in a synchronized state in the wrapped and unwrapped diagrams respectively. Panels on the right show the corresponding interpretations as over-damped particles moving in tilted washboard potentials. (a) Slow-fast coupled motion, described by the regime of the Adler equation where $k < |\Delta\omega|$. Insets in the left panel show images of the measured cells at the frame in the recording corresponding to the time point in the diagram. (b) Switching between in-phase and anti-phase synchronization, driven by periodic kicks. (c) In-phase synchronization with periodic kicks, corresponding to the regime of the Adler equation where $k > |\Delta\omega|$.

12

5 Discussion

In 1665, Dutch scientist and father of the pendulum clock Christiaan Huygens famously for the first time reported about the tendency of objects to move in harmony [44]. Two clocks suspended from the same wooden base would over time reach a state of synchrony, in which each pendulum swung simultaneously in opposite direction, what is known today as anti-phase synchrony. While Huygens' observation went by relatively unnoticed at the time, synchronization has become a relevant topic in recent decades and has captured the interest of the scientific community. From the collective movements of schools of fish and bird flocks that collectively swirl and turn to avoid predators [45], to the synchronized flashing of fireflies [46], and even to the spontaneous synchronized clapping of theater audiences [47]. Here, we report the first evidence of controlled synchronization between single bacterial cells, taming their random-like behaviour, and proving synchronization to appear even at the smallest (micrometer) scale.

Despite numerous previous experimental studies investigating micro-swimmers in bulk or on open PDMS structures, the specific type of collective behaviour we report here has never yet been observed. Works exploring the ordering of *E.coli* vortices in connected microwells showed that cells would distribute uniformly inside the structures, indicating that hydrodynamic surface entrapment may be suppressed in dense bacterial populations [14][39]. Moreover, the alignment of vortex spins would depend on the channel width, determining whether or not cells could swim through. Here, by further decreasing the size of cavities, and working with low concentrations of bacteria, we developed arrays of single cell bacterial oscillators performing periodic clockwise rotations. We demonstrate hydrodynamic surface entrapment to be the driving factor behind cell trapping, as measurements of cells in inverted cavities would reveal *E.coli* to overcome gravity and swim along the ceiling (Supplementary 8.7). Furthermore, by devising sets of microcavities connected by on-chip channels, we showed *E.coli* tend to coordinate their motion, and exhibit coupled oscillatory motion. Our results suggest that microchannels could be designed to induce a rich variety of dynamical behaviors between cells, driven by long-range hydrodynamic interactions. Moreover, our method of cell trapping was observed to induce clockwise rotations of cells not only in circular microwells, but also in various other geometries such as rectangular traps and square labyrinths. (Supplementary 8.8).

We foresee applications for arrays of single cell bacterial oscillators in the design of controllable microfluidic mixers, expanding on simulation studies exploring networks of microorganisms-based oscillators [48]. The technology could moreover be utilized in the advancement of rapid antibiotic screening methods, where the highly localized periodic motion of living cells could potentially provide significant benefits. In the recent work by Rosłoń, I. et al. (2023) [49] involving the optical detection of single motile *E.coli*, cell viability was measured by focusing a laser at a predetermined spot on a patterned surface. As such, by engineering traps to increase the frequency at which bacteria pass the laser light, new avenues could be opened for fast antibiotic susceptibility testing.

6 Methods

6.1 Method of fabricating microcavities

In order to gain any insight in the influence of cavity size on bacterial motion, it is necessary to collect a sufficient amount of swimming data in each geometry. For the fabrication of substrates this means it is desirable to have a method to quickly produce large arrays of identical microcavities. Moulding is one of the most common manufacturing processes for producing uniform plastics (among others). Generally moulding makes use of a rigid, high stiffness frame, also called mould, that is given the exact inverted shape from the desired end product. Liquid plastic is then injected, which upon curing hardens to the configuration of the mould. Besides being a popular manufacturing processes in industry, moulding has also been shown an effective method for producing microfluidic devices for bacteria [25]. The process used here for making microcavities to trap *E.coli* generally works in a similar way. In this section this process will be explained more extensively.

6.1.1 Wafer patterning

In order to end up with a microfluidic structure with hollow circular microcavities, first a master is manufactured with the exact inverted shape. This is done by means of dry-etching, a multi step process which is able to etch details with nanometer accuracy [50]. The master consists of a silicon (Si) wafer, with a 280 nm surface layer of silicon dioxide (SiO2). Dry-etching is performed by the Kavli nanolab, a research facility at TU Delft for nanofabrication. On the wafer surface multiple arrays of micropillars are patterned, every array with a specific pillar diameter. Figure 5 shows a scanning electron microscope (SEM) image of the patterned wafer surface.
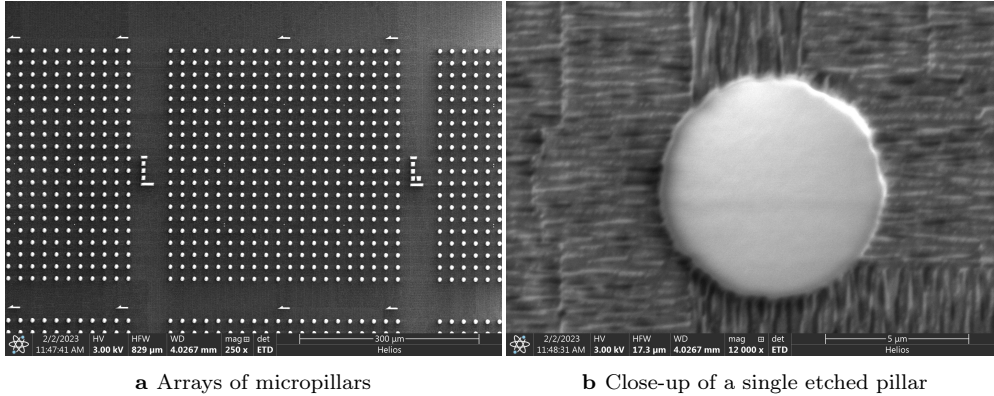

a Arrays of micropillars   **b** Close-up of a single etched pillar

Figure 5: SEM images of the pattered wafer

6.1.2 Silanization

In the process of preparing a wafer for use, it is necessary to apply a lubricating surface coating in order to ensure that the mould can be easily released after it has been cured. In this particular case, we opted to use (Tridecafluoro-l,l,2,2-tetrahydrooctyl)trichlorosilane (FTS) as silanization reagent, which has previously been found to form low-friction monolayers on

silicon devices [51]. To apply the FTS coating, an open container containing a few droplets of FTS was placed together with the patterned wafer in a closed vacuum chamber for 15min. During this process, the FTS vaporized, and the resulting molecules formed covalent bonds with silicon, resulting in the formation of a thin lubrication film on the wafer surface. It is important to note that wafer silanization should be performed periodically every ∼10-15 release cycles. While the coating is initially applied as a finishing treatment in the wafer preparation process, periodic re-application ensures that it continues to act as an effective lubricant for the mould.

6.1.3 Substrate preparation

A widely used polymer for fabricating microfluidic devices in cell biology is Polydimethyl siloxane, or PDMS in short. PDMS is a mineral-organic polymer that is usually liquid at room temperature, but when mixed with a cross-linker (curing agent) and heated becomes a rubber-like solid. Its transparency at optical frequencies, strong adhesiveness to glass and ability to be moulded with nanometer resolution [52], makes PDMS a very suitable material for making microcavities to measure bacterial motility in confinement. Figure 6 highlights the process used for fabricating PDMS substrates.
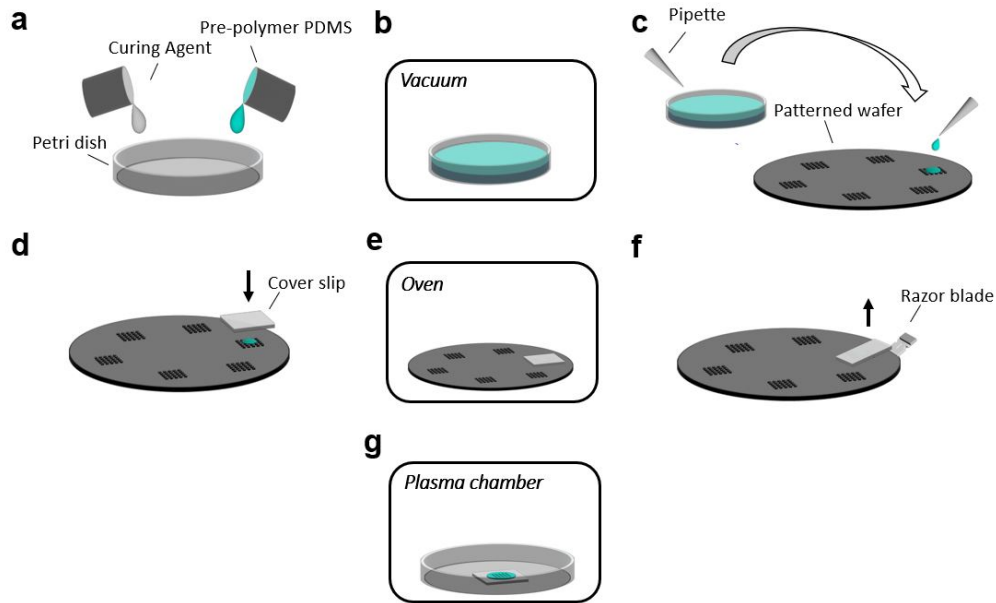

Figure 6: The process of fabricating PDMS substrates with microcavities, PDMS is colored green for visibility. (a) Liquid pre-polymer PDMS is mixed with a curing agent and thoroughly stirred. (b) The mixture is placed under vacuum until visibly all air-bubbles are removed. (c) A droplet of PDMS is dispensed on each of the patterned structures on the wafer, for explanatory reason here just one is shown. (d) By placing a glass cover slip on top, the droplet spreads out over the patterned wafer structure and ends up covering it entirely. (e) The assembly is placed inside an oven to cure the PDMS film sandwiched between cover slip and wafer. (f) With a sterile razor blade the cover slip is carefully lifted from the wafer. The PDMS layer adheres stronger to glass than the silanized wafer surface, and thus releases completely from the patterned structure. (g) Finally the substrate is placed, PDMS side up, in a plasma chamber to be surface treated by oxygen plasma.

Part of the utility of PDMS in producing microfluidics lays in the aspect that its mechanical, physical and tribological properties are adjustable, in particular through altering curing agent mixing ratio and the type of heat treatment used for curing [53]. This allows researchers the flexibility to conjure up the best suited recipe for their specific application. For microcavities 2.5 μm deep and 5-30 μm in diameter we found, through trial and error, that pre-polymer PDMS : curing agent mixing ratio of 4:1, along with heat treatment of 2.5 hours at 90 ^{o}C (in the oven) is suitable. After curing the substrate is lifted by carefully wedging a sharp sterile razor blade between wafer and glass slide, as shown in figure 6 (f). For this lifting technique it is important to have at least one PDMS-free corner underneath the slide to function as starting edge for the blade. For a slide of $22x22mm$ that means the volume of PDMS dispensed on the patterned structure should be approximately 1 μl. A picture of the assembly just after curing is shown in figure 7. To lift the substrate the blade is simply moved upwards, which creates the required peeling forces for the PDMS layer to slowly release from the wafer.
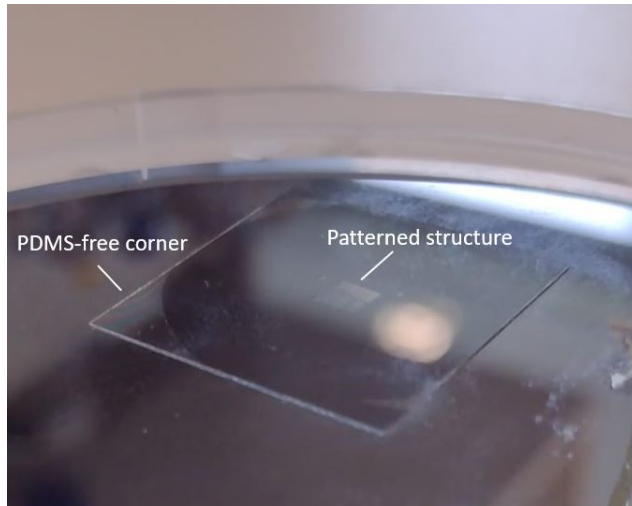

Figure 7: Picture of PDMS substrate on the wafer after curing. In the center of the substrate lays the patterned structure as indicated. The PDMS-free corner is used as starting edge to peel the substrate off

Finally, in order to allow the water based bacterial solution to fill the microcavities it is necessary to overcome the hydrophobic nature of the PDMS surface. A proven way to do so is by oxygen plasma surface treatment. Exposure to oxygen plasma temporarily turns the initially hydrophobic PDMS surface hydrophilic. However, while after being exposed to oxygen plasma PDMS reaches hydrophobic recovery within time, prolonged plasma treatment causes cracks to grow and irreversibly deteriorates the surface [54]. It is found that at $20W$ plasma power and $60mTorr$ oxygen chamber pressure, exposure for 30 seconds is enough for the PDMS surface to remain hydrophilic for several hours.

6.2 Substrate geometry

6.2.1 Pattern design

Two separate patterned wafers have been used for the fabrication of substrates for experiments on bacterial trapping. Wafer A was equipped with arrays of $1.5\mu m$ protruding micropillars with diameters ranging from 5-$8\mu m$, whereas wafer B was etched to $2.5\mu m$ depth and hosted both micropillars with 8-$30\mu m$ diameter, as well as dumbbell structures. Both silicon wafers were patterned following the same dry-etching process (see section 6.1.1). Dumbbell structures in this context consist of a symmetric pair of bridged micropillars, which were fabricated with pillars ranging from 5-$10\mu m$ in diameter and bridges of 0.5-1-$2\mu m$ length and 0.5-0.7-$0.9\mu m$ width. Figure 8a shows a microscopic image of the complete $3x3mm$ patterned structure on wafer B, with zoomed-in views in fig 8b-c.

a Complete overview of the patterned structure

b Close-up corresponding to the inset shown in (a)

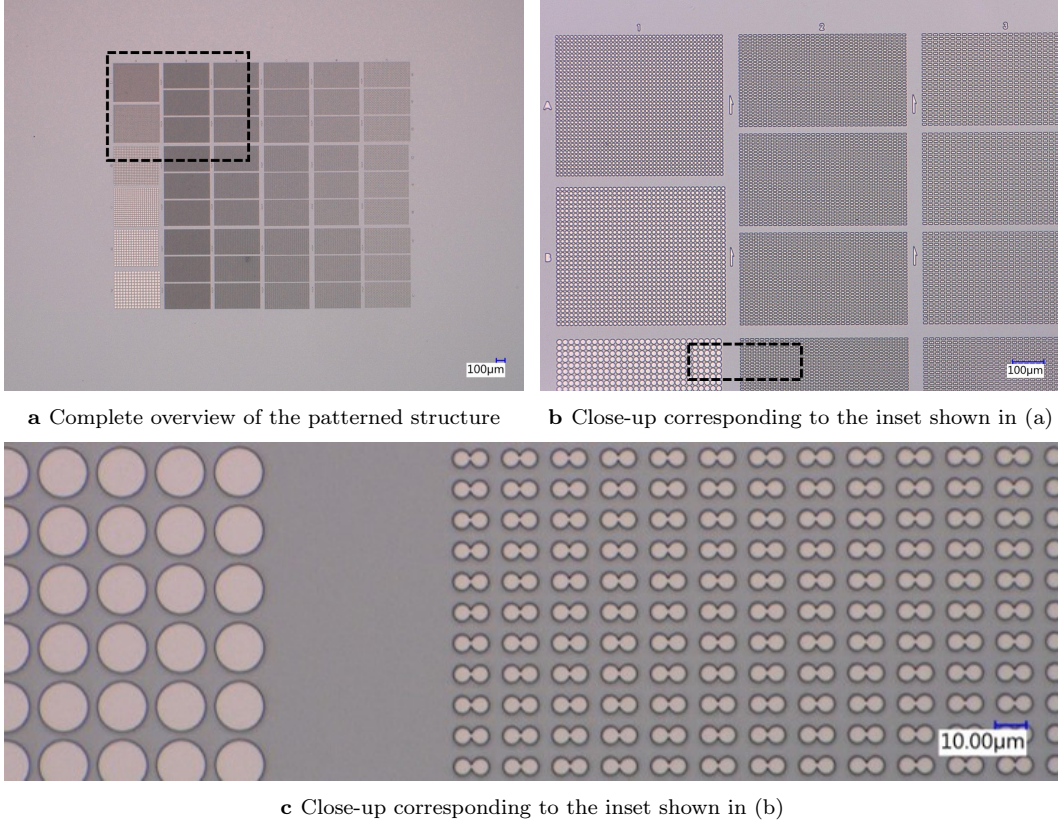**c** Close-up corresponding to the inset shown in (b)

Figure 8: Images of the patterned structure on wafer B acquired by optical (Keyence) microscope.

Figure 9 draws a broad overview of the structure designs (left panels) compared to the etched wafer patterns (middle panels) and the resulting traps on the substrate (right panels). Micropillars on both wafers A and B were designed to be spaced $4\mu m$ apart, regardless of pillar size 'd' (see left panel of fig 9a). Under 100x magnification, translating to a microscopic field of view of $\sim$133x133μm, this meant up to 225 cavities of $d =5\mu m$ could be measured simultaneously, whereas up to 16 cavities of $d =30\mu m$. Dumbbell structures were designed to be spaced a pillar diameter from one another (see left panel of fig 9b), in order to negate potential hydrodynamic interaction between cells trapped in different pairs of connected cavities.
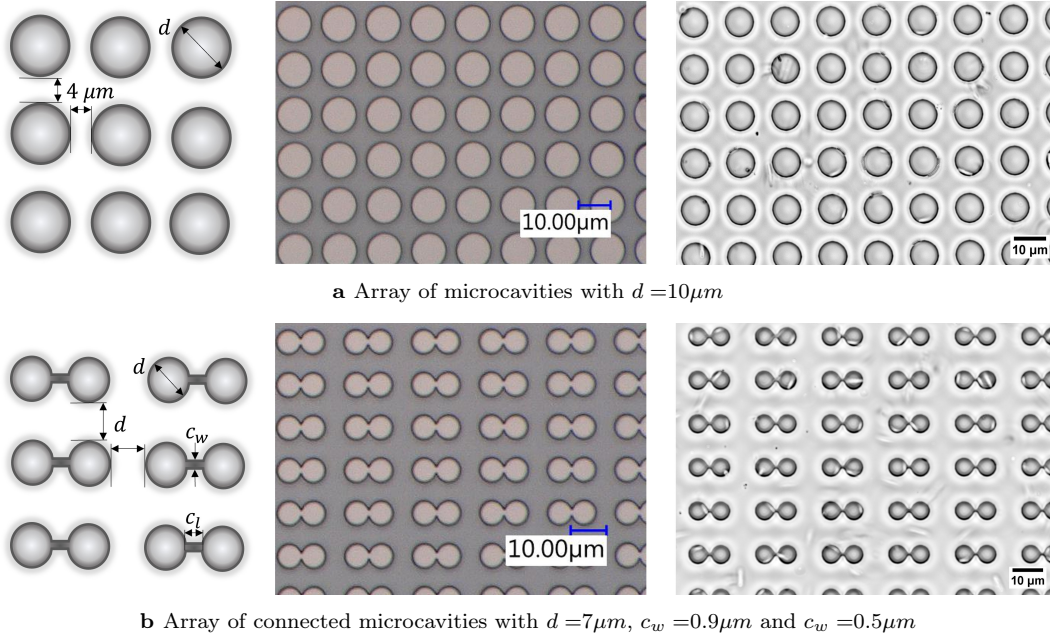

a Array of microcavities with $d =10\mu m$

b Array of connected microcavities with $d =7\mu m$, $c_w =0.9\mu m$ and $c_w =0.5\mu m$

Figure 9: Comparison of structure designs to the patterned wafer arrays and the resulting arrays of traps on the PDMS substrate. Panels show schematics of array dimensions (left), etched wafer patterns (middle) and corresponding traps on the PDMS substrate (right).

6.2.2 Manufacturing accuracy

Previous sections explained all the steps taken in the preparation of a patterned PDMS substrate. It is known from the dry-etching process that details can be etched with nanometer accuracy. However, how curing, the method of peeling off the substrate from the wafer, or surface plasma treatment affects the final PDMS pattern dimensions cannot be known beforehand. For this reason we investigated the final reached substrate manufacturing accuracy from images gathered by the setup shown in figure 1a. To analyse image information and detect features such as cavities and cells, a custom image processing algorithm has been developed. How this algorithm works is explained more extensively in section 6.4.1.

From several PDMS substrates used over multiple cell motility measurements, cavity sizes are measured via automated object detection. The diagram in figure 10 shows the range of measured PDMS cavity sizes.
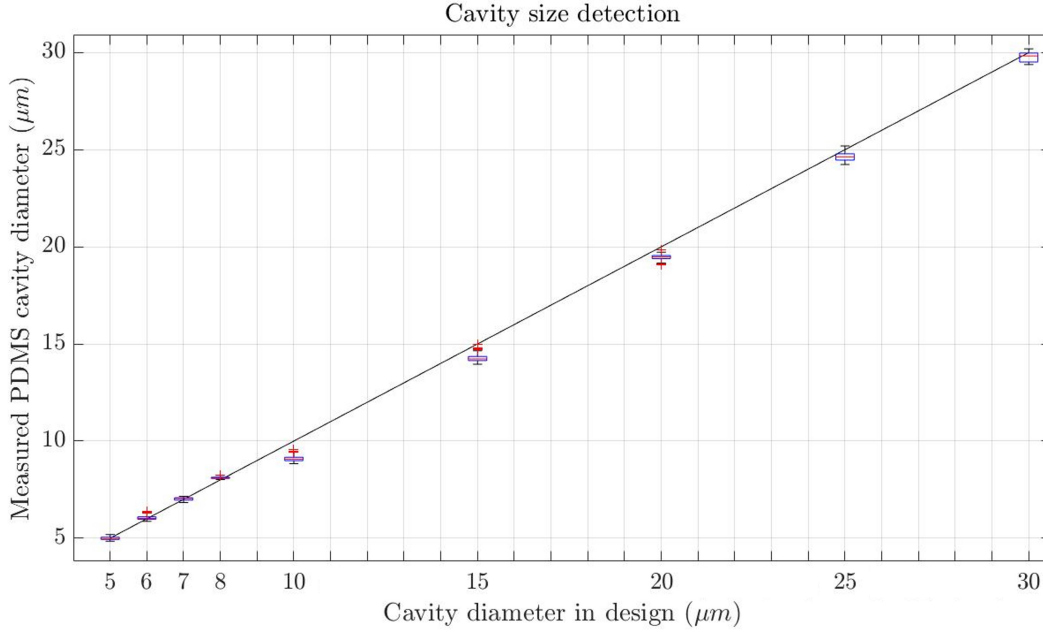

Figure 10: Cavity sizes measured through object detection versus intended diameters by design. Proximity to the diagonal institutes high manufacturing accuracy

It should be noted that the gathered measurements on cavity sizes are subjective both to manufacturing inaccuracies as to measurement noise of the object detection algorithm. As such it is not possible to, based on the data shown in figure 10, deduce any absolute achieved manufacturing accuracy. What can be judged instead are trends and discrepancies in the data. It should be noted furthermore that the 5-8μm cavities were patterned on a different wafer than the 10-30μm cavities, following the same dry-etching process.

From the figure it can be seen in the 5-8μm domain, the measured cavity diameters lie

fairly close to the diagonal, with medians within 0.1 μm bounds of the design diameter, see also table 1 below. Although what also can be observed, is that the larger cavities are more off, with the offset remarkably growing smaller with increasing cavity size. This offset could have been caused either by some inaccuracy in the substrate fabrication process, or through a detection error in the software, or both. However, since the offset is more than measured at 5-8μm cavities, though being measured by the same software, it is hypothesized that the measured diameter offset is accurate. More important however is the measured deviation in cavity sizes, which especially when keeping in mind the image resolution of 0.065μm/pixel is reasonably small over the entire domain. This is why going forward, following the observations made in this section, the next assumptions will be made:

- The 10μm designed cavities will be regarded as 9μm
- The 15μm designed cavities will be regarded as 14μm
- The 20μm designed cavities will be regarded as 19μm

Cav Diameter	#Measurements	Mean $\pm$ std (μm)	Rel mean offset
5μm	608	5.0 $\pm$ 0.07	0.30%
6μm	506	6.0 $\pm$ 0.01	0.66%
7μm	424	7.0 $\pm$ 0.07	0.36%
8μm	361	8.1 $\pm$ 0.05	1.3%
10μm	324	9.1 $\pm$ 0.14	9.0%
15μm	304	14.3 $\pm$ 0.17	4.9%
20μm	160	19.5 $\pm$ 0.13	2.7%
25μm	124	24.6 $\pm$ 0.22	1.5%
30μm	100	29.8 $\pm$ 0.24	0.78%

Table 1: Manufacturing performance parameters. Table lists measured cavity diameters compared to the intended sizes as per design.

Similarly as holds for the cavity diameters, it is unclear how the method of preparing PDMS substrates affects the depth of the final PDMS cavities. Same as has been done for measuring cavity diameters, a PDMS substrate is analysed after undergoing plasma treatment (the last step in the preparation process, also shown in figure 6). By observing the substrate with a scanning electron microscope (SEM) the actual achieved cavity depth can be measured, as shown in figure 11. The substrate is tilted to an angle of $\alpha =$30deg (figure 11a), which allows the observer to see the slanted cavity wall. What can be measured from the image is denoted in figure 11a as 'x'. From simple trigonometry then the actual cavity depth 'd' can be derived, see also equation 2.

$$d = x/sin(\alpha) \tag{2}$$

For a number of cavities in different areas of the substrate the 'x' is manually measured through image processing software, as shown in figure 11b. The cavity depths annotated in the image have readily been converted to actual cavity depths 'd'.
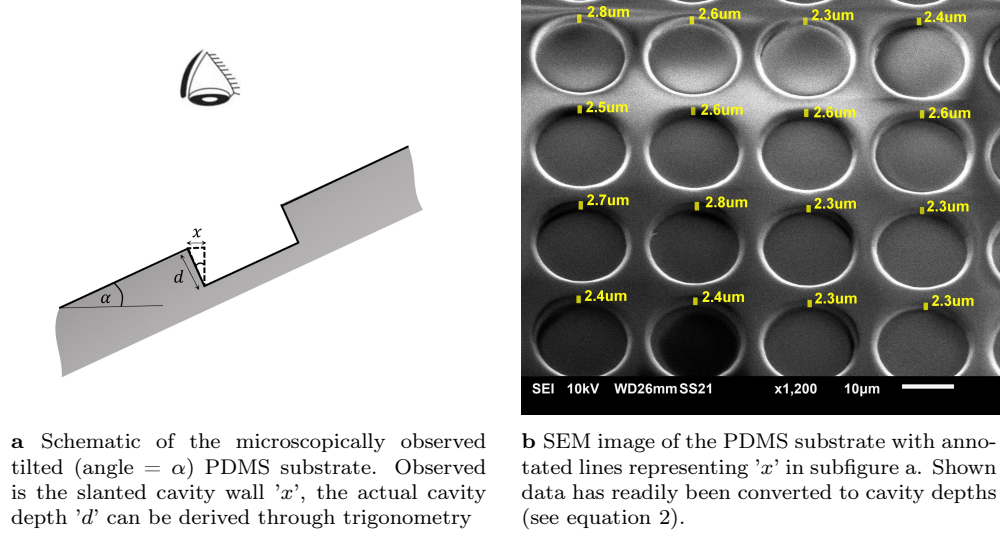
a Schematic of the microscopically observed tilted (angle = α) PDMS substrate. Observed is the slanted cavity wall 'x', the actual cavity depth 'd' can be derived through trigonometry

b SEM image of the PDMS substrate with annotated lines representing 'x' in subfigure a. Shown data has readily been converted to cavity depths (see equation 2).

Figure 11: Method of measuring cavity depths

What stands out in the substrate images is the occasional appearance of PDMS wrinkles, which often are situated in spaces between cavities. Such a wrinkle can be observed as well in the top left corner of figure 11b. It is most likely that during substrate preparation, by placing the cover slip (figure 6d), the wafer pattern presses into the thin PDMS layer, causing excess PDMS to accumulate around the cavities. The pattern on the substrate is thus likely not surrounded by a perfect flat surface as depicted in figure 11a, but instead cavities are separated by inflated boundaries.

Figure 12 shows the range of measured cavity depths on the PDMS substrate. As can be seen the mean lies just below $2.6\,\mu m$, which is fairly close to the aimed $2.5\,\mu m$ to which the dry-etching process was tuned. It is hypothesized that the inflated boundaries may cause the cavities to appear deeper in the microscopic images, which explains the offset in mean. The deviation in depths could possibly have been caused by the inaccuracy of manual measurement, or the PDMS wrinkles which are not necessarily equal in height across the substrate. Both are not expected to have any influence on bacterial swimming inside the cavities and thus will not be regarded in further analysis.
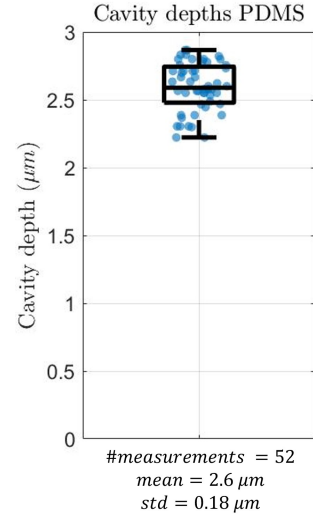

Figure 12: Boxplot of measured cavity depths, scattered data points are added in overlay

6.3 Experiments

Cell culture Smooth sailing *Escherichia coli* (cheA strain) were grown in Lysogeny broth (LB). A monoclonal colony was diluted in 5ml LB and left to grow overnight at 30^oC while gently stirred in an incubator. On the day of the experiment, an $50\mu l$ aliquot was diluted 1:100 into 5ml LB and grown for 2.5 h at 30^oC to mid-exponential phase. A subsample of this culture was again diluted between 1:5 and 1:10 in LB to finally reach an optical density (OD) of 0.05.

Substrate preparation Pre-polymer PDMS was mixed with curing agent in 4:1 ratio (2g PDMS to 0.5g curing agent), and stirred manually with the tip of a sterile pipette. The mixture was then degassed in a vacuum chamber for 10-15 min, until by eye all air bubbles had disappeared. Using the tip of a pipette, a small amount of PDMS was carefully dipped in the center of one of the structures of the patterned wafer (see Methods 6.1.1). Then, a 1mm thick, 22x22mm glass slide was placed on the droplet, spreading it over the patterned wafer structure. The assembly was subsequently baked at 90^oC for 2.5h in an autoclave. With a sharp sterile razor blade, the glass slide was carefully lifted from the wafer and plasma treated at 20W plasma power and 60mTorr oxygen chamber pressure for 30 s.

Imaging For imaging, about 35 μl cell culture was pipetted onto a prepared PDMS sample and placed on a larger sample holder. Then, with parafilm we placed a sample cover over the PDMS sample, creating a sealed chamber (see fig 1a). The assembly was placed inside a closed microscopic chamber maintained at 30^oC. Observations were made using an inverted microscope (Nikon Ti) under bright-field illumination, through a $100\times$ oil-immersion objective. Recordings typically had 2min duration at frame acquisition interval of 0.23s.

6.4   Measuring cell motion in cavities

When cells become trapped in a circular microcavity they seem to systematically swim along the wall in clockwise direction, as has been explained in section 6. In order to analyse how this rotary motion of cells is affected by the cavity size, it is necessary to have a method to track cell motion in an automated way. There exist already various cell tracking tools which are able to detect cells and track their position over time. Some of them using complex algorithms meant to segment individual cells from a cluster [55], or to track swimming cells which can suddenly turn and bump into neighbours [56]. Otherwise when there is a high degree of overlapping or a certain variability in cell phenotype, several machine learning techniques have been applied and shown to perform well [57][58]. The benefit of the way of measuring confined bacterial motion presented here however, is that it removes much of the programming complexity surrounding clustering and overlapping. Here considered microcavities contain only a single physically isolated cell, of which the shape features are known beforehand. For this reason it is chosen to develop a custom tracking algorithm, which is able to track the motion of individual cells inside cavities. This section elaborates on how this algorithm works.

6.4.1   Cell tracking

From the moment that the bacterial suspension is dispensed over the PDMS substrate, cells by gravity and surface attraction settle down inside the microcavities and become trapped. The goal of the image post processing software is to track cell movement while cells are trapped inside a cavity. The first task at hand is thus to find all cavity locations in the microscope recording, to afterwards find the positions of each cell that may reside inside. A few simplifications can furthermore be made. Since already a single 2 minute microscope recording of cell trapping consists of approximately 600 images, finding both cavity and cell locations in each frame quickly becomes computationally intensive. Each frame is taken on the same substrate location however, thus assuming negligible camera drift it is enough to measure cavity positions only once for each recording. Furthermore, since here the dynamics of physically isolated cells in confinement is investigated, instances were multiple cells are found inside the same cavity can be discarded. That means that cell segmentation, an usually challenging task in cell tracking, does thus not have to be considered.

In summary the strategy for cell tracking is as follows: First cavity positions are derived from the first frame of the recording. Then for each found cavity, in case there is a single cell detected inside, the position of the trapped cell is measured with respect to the cavity center. The latter being repeated for each frame for the duration of the recording. Figure 13 gives an overview of the cell tracking process.
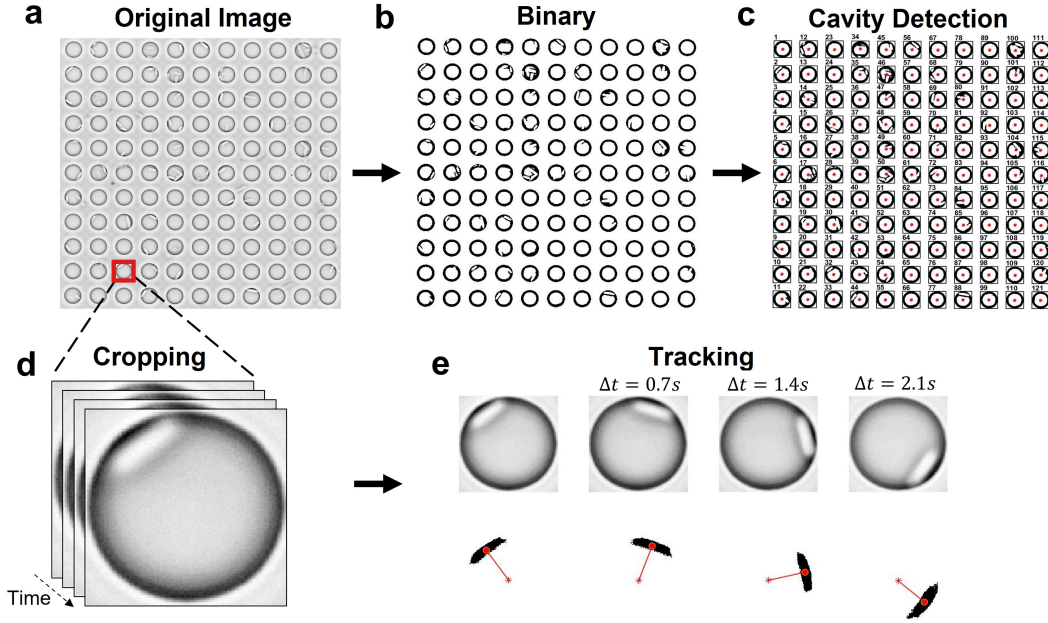
Figure 13: Flowchart of the cell tracking process. (a) A single frame taken from the microscope recording of the microcavity array. (b) Original image is converted to binary by applying a pixel intensity threshold. (c) Objects are identified as cavities from which both the geometrical center (red stars) and size can be measured. (d) When all cavities are found take cropped images of each cavity for every frame of the recording. (e) Detect cells residing inside the cavity and in case a single cell is found track its position over time

Generally with object detection algorithms in image processing it is necessary to find a feature that differentiates the object in question from its surroundings. In case of the cavities in the microscopic image shown in figure 13a, it stands out that each cavity boundary is accompanied by a distinct dark ring. This area lining the inside of the cavity border apparently has very different light reflection properties than other parts of the substrate, which offers opportunity for detection. The tracking software takes advantage of this feature by application of a pixel intensity threshold, which filters pixels belonging to dark cavity rings from the background and converts the original image to binary (figure 13b). In the binary image the only remaining pixels are those which make up cavity rings. Next, chains of connected pixels can be given a specific label which in turn creates objects. Pixels with label 1 make up one object, pixels labelled 2 make up another, and so on. From each created object the location of the geometric center in the image is calculated along with the height and width, figure 13c shows the end result. These are the cavity specifics that are computed once only for every recording to be then stored in a table. As final step it is checked for each found object whether derived dimensions lie in margin of what was expected from the known cavity diameter. Objects that do not comply are discarded, whereas objects that do can be considered for further tracking purposes. At these object locations portions are cropped from the image corresponding with single cavities. This process is then repeated for every frame in the recording, as shown in figure 13d. Ultimately for every frame of a cavity a second specialized detection algorithm looks for residing cells, and measures the

position of their center of mass with respect to the cavity center. Figure 13e depicts a series of cavity frames in which a cell is found and tracked.

The detection of cells inside cavities is done in similar manner as the detection of cavities in the array. Figure 14 draws an overview of the process.
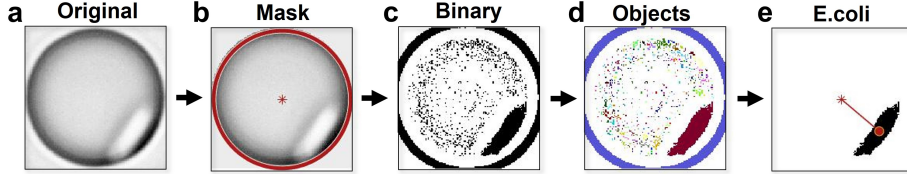

Figure 14: Flowchart of the cell detection process. (a) Image of a single cavity cropped from the array. (b) Image after application of a mask with annotated detected cavity edge (red ring) and cavity center (red star). (c) Conversion to binary through a pixel intensity threshold. (d) Groups of connected pixels labeled as objects with pseudo random colors. (e) The object representing an *E.coli* cell is filtered from the cluster and its center of mass measured relative to the cavity center

From a portion of the original microscopic image cropped around a single cavity (figure 14a), the goal is to detect any potential residing cells and find their position with respect to the cavity center. First, based on a circular Hough transform, a common feature extraction technique for finding circular features in imperfect images [59], the algorithm detects the edge of the cavity in consideration. In this way both the radius and geometric center are measured in a more sophisticated way than was done in the coarse cavity detection process elaborated in figure 13. Once the cavity edge is found, a mask is applied which clears the corners of the image which lie outside the cavity. In this way, cells which may have appeared in the cropped image but were not trapped are excluded from being detected. The found cavity edge and geometric center are annotated in the mask image in figure 14b as a red ring and marker respectively. Next, since *E.coli* cells appear as the brightest feature in the image, a basic pixel intensity threshold can be applied to convert the image to binary, shown in figure 14c. Connected pixels are sorted into objects, labeled with pseudo random colors in figure 14d. Making use of the known typical shape characteristics of *E.coli*, e.g. its cylindrical shaped cell body and roughly 2 μm^2 size, the bacterium is finally filtered from the cluster of objects. The position of the bacterium's center of mass relative to the cavity center is then measured and stored, as shown in figure 14e, after which the next frame is loaded to repeat the process from start.

6.4.2 Crowded cavities

Previous section elaborated on the general structure of the cell tracking process. Cells can be detected by utilizing the difference in pixel intensity with the background. In practice however, cavities may contain multiple trapped bacteria, which adds complexity to the measurement. In the case of a cavity with multiple residing cells, the tracking algorithm in addition to detecting cells, is required to distinguish between cells when computing swimming trajectories.

Multiple cells trapped simultaneously in the same microcavity may potentially influence each others movement. Since physical cell-cell interaction is an unwanted factor in studying the relation of cell motility to cavity size, there is no need to equip the tracking algorithm with tools to distinguish between cells. Cropped microcavity images in which more than one cell are detected are therefore omitted from further analysis. In cavities with a diameter less than the typical size of $E.coli$ including flagella (approx. $10\mu m$), this measure has been found to not significantly affect the quality of tracking data. Cavities of this size often host a single cell, and at times where a second cell jumps in, one of the two is often quickly forced out. However, with increasing diameter, cavities on average become more crowded, and limiting the analysis to cavities with a single trapped cell renders most measurements unusable.

Thus, in order to work around the problem of crowding in large wells, only the number of detected cells that swim along the cavity wall are counted. Instances where a single cell is detected at the cavity edge are considered for further analysis, whereas measurements where multiple cells are found in this area are discarded. Table 2 draws an overview for the strategy used to distinguish between measurements fit for further consideration, and measurements to be discarded.
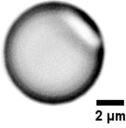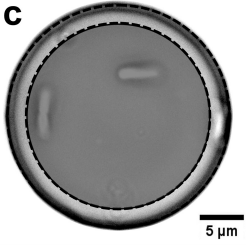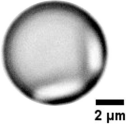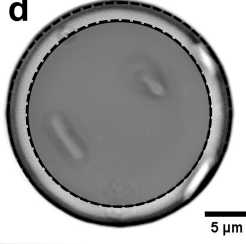
	$d \leq 10\mu$m	$d > 10\mu$m
Consider	**a** 2 µm	**c** 5 µm
Discard	**b** 2 µm	**d** 5 µm

Table 2: Overview of considered measurements versus discarded ones for cavities with diameter 'd' $\leq 10\mu m$ and $>10\mu m$. (a) A cavity ($d = 7\mu m$) with a single trapped cell. (b) A cavity ($d = 7\mu m$) with multiple trapped cells. (c) A cavity ($d = 25\mu m$) with multiple trapped cells, but only a single one located at the edge, outside of the area annotated with the dark circle. (d) A cavity ($d = 25\mu m$) with multiple trapped cells, having multiple cells located at the cavity edge

For cavities $>10\mu m$, the dark circles displayed in table 2 are centered with the cavity and set to a diameter of 80% the cavity diameter. For the measurement to be considered, there must be exactly one cell detected with a centroid outside the circle of occlusion.

6.4.3 Data segmentation

Over the duration of a typical 2 minute recording of a microcavity it is possible that the gathered tracking data consists of different cells that have been trapped subsequently. In order to extract information about individual cells we therefore aimed to segment cell tracking data into individual cell runs. To achieve this, we used a segmentation method that involved computing median anchors for every 20 velocity data points. If the gap between anchors was more than 1.5 times the velocity standard deviation, or if the gap between velocity points was more than 10 seconds, a break was inserted in the data, as shown in figure 15. This ensured that the data was broken up into segments that corresponded to distinct periods of cell movement. For each data segment, we further checked whether the tracked cell was swimming by examining the phase slope. Specifically, we checked that the phase slope was negative at least more than 75 percent of the time. This check was important to ensure that we were only analyzing data from periods when the cell was actively swimming along the cavity wall, as opposed to when it was stationary or twitching due to becoming stuck.
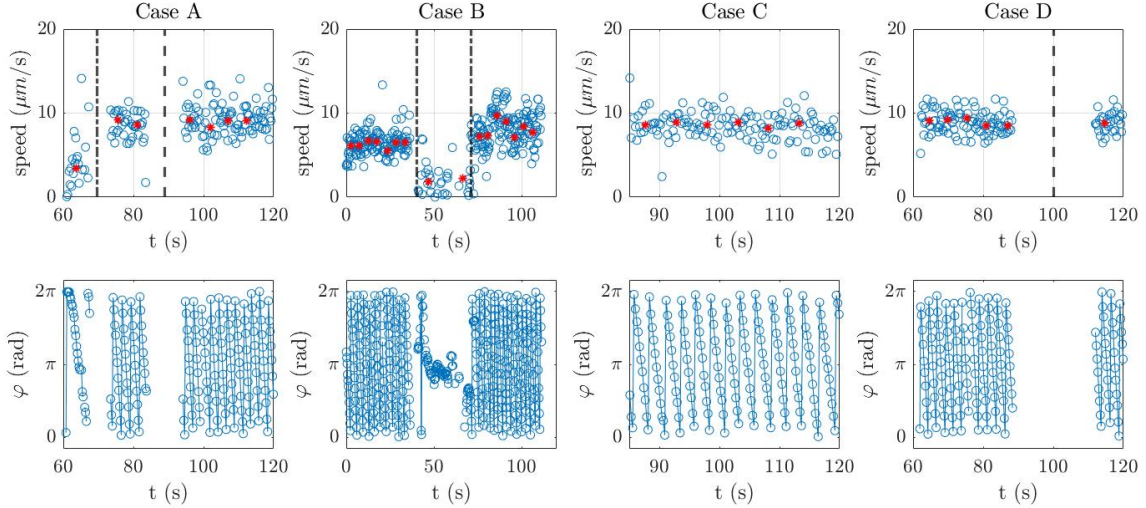
Figure 15: Four examples of how cell tracking data is analyzed and segmented, implementing the coordinate system displayed in fig 1b. The top row diagrams show cell speed (in scatter) over time, with the corresponding cell phase angle on the bottom row. Breaks are inserted where the gap in median anchors (red markers) is more than 1.5 times the standard deviation (dashdotted black line), or where gap between velocity points was more than 10 seconds (dashed black line).

6.4.4 Bacterial activity

To measure bacterial activity in cavities and generate heatmaps (see fig 2b), we analyzed recordings of 144, $7\mu m$ cavities by method elaborated in section 6.4.1. The algorithm segmented traces into trajectories of 6 seconds and checked that cells were moving by verifying that the measured motion variance (see eq 3) was greater than 1.3 μm^2. Here n is the number of frames in the video sample, x_i denotes the measured cell x position at frame i, and $\hat{x}$ the cell's mean x position over the trajectory. Upon deriving the variance in the y position in a similar fashion, the total variance can then be characterized by $Var = \frac{1}{2}(Var_x + Var_y)$.

$$Var_x = \frac{1}{n} \sum_{i=1}^{n} (x_i - \hat{x})^2 \tag{3}$$

To analyze data from $25\mu m$ cavities, the ImageJ module TrackMate was used to process recordings from 9 cavities. Only trajectories of swimming cells were considered, verified by their distance travelled and a low mean directional change rate. From the cell x/y coordinates, the distance from the cell to cavity center was derived as 'r'. Trajectories were stitched together to generate a single continued trace, and cells were considered 'at the wall' when they were at most $2\mu m$ from the cavity wall. Figure 16 shows the resulting time traces for both considered cavity sizes, with the area between horizontal red lines indicating where cells are considered at the wall. In $7\mu m$ cavities, averaging over 271 trajectories of cells which swam for 6 seconds, we found 99% of motion to be concentrated by the cavity wall. Whereas for $25\mu m$ cavities we derived, by averaging over 92 trajectories, that cell motion was for 77% distributed by the cavity wall.
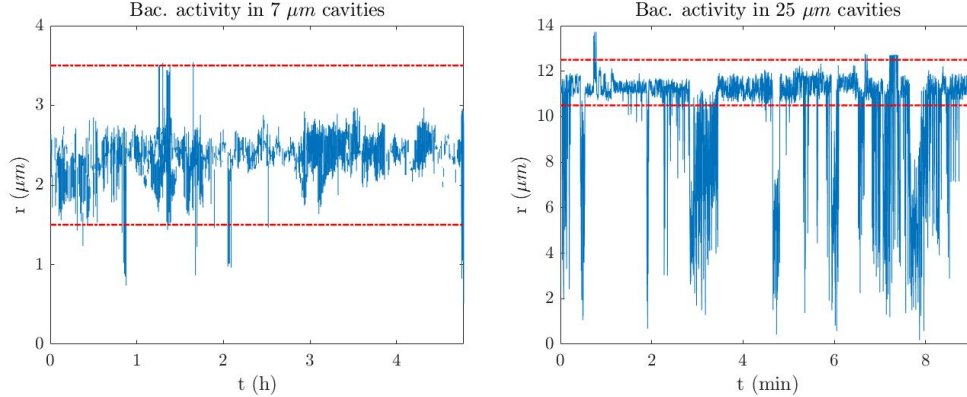

Figure 16: Bacterial activity in $7\mu m$ (left panel) and $25\mu m$ (right panel) cavities. The time traces (in blue) represent stitched trajectories from different swimming cells. The dashdotted red lines indicate the area where cells are considered to be swimming by the cavity wall

7 Theory

7.1 Slow-fast dynamics of coupled cells

In the previous sections circular microcavities have been demonstrated a useful tool to transform single bacterial cells into trapped rotators. Inherently chaotic bacterial motion can be reduced to ordered circular trajectories, and cell speed can be controlled by means of tuning the cavity diameter. In this way, circular cavities induce limit cycle oscillations of isolated trapped cells that are sustained for up to several minutes. Now, by connecting microcavities with on-chip channels, see figure 17, we engineer coupled traps that are more facilitating to fluid flow between individual trapping sites. In this way, we increase the potential of cells sensing hydrodynamic forces created by swimming neighbours, and induce slow-fast dynamics.
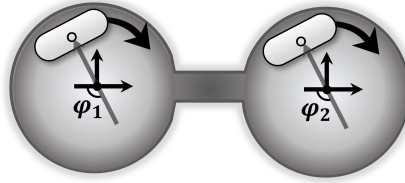
Figure 17: Schematic of coupled cavities connected by a channel. Phases of cells are measured with respect to the center of the cavity they are trapped in respectively.

A pair of cells are stated to be synchronized when their phase difference, $\varphi_1 - \varphi_2$, remains zero over time. In practice however, perfect indefinitely sustained synchronization does not occur in nature, as it requires a system of perfectly identical oscillators. Even pairs of synchronized metronomes have been reported to over time return to out-of-phase ticking because of small differences in intrinsic frequencies [60]. Similarly, no two cells of *E.coli* are the same, and as such we assume synchronization to be strictly of temporary nature.

Neighbouring cells of *E.coli* trapped in coupled microcavities are observed to periodically reach states of in-phase and out-of-phase swimming with a slow-fast dynamic. Cells tend to swim for prolonged periods of time in-phase, and out-of-phase behave as two oscillators with constant frequency difference. Figure 18 shows measured time traces of the phase difference between two cells in regular cavities and in cavities connected via on-chip channels.
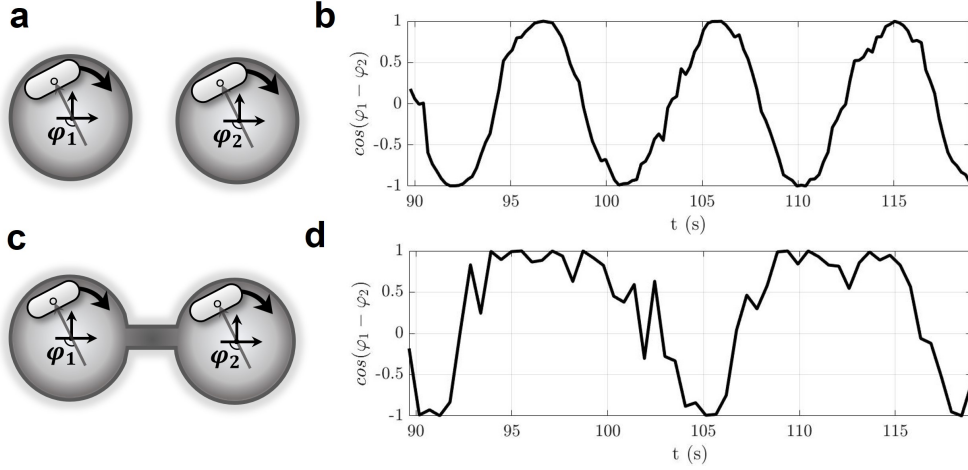
Figure 18: Phase differences of neighbouring cells in cavities with and without a channel. (a) Schematic of cells in uncoupled cavities. (b) Measured phase difference of two cells in uncoupled cavities. The cosine of the phase difference is displayed on the y-axis to show the absolute normalized value. $Cos(\varphi_1 - \varphi_2) = 1$ indicates cells are in-phase, whereas $cos(\varphi_1 - \varphi_2) = -1$ points to cells being in anti-phase. Tracking was carried out by the tracking algorithm discussed in section 6.4.1. (c) Schematic of cells in coupled cavities. (d) Measured phase difference of two cells in coupled cavities. Tracking was performed manually with ImageJ.

For two uncoupled rotators with constant intrinsic frequencies the cosine of the phase difference can be rewritten as shown in equation 4.

$$cos(\varphi_1 - \varphi_2) = cos((\dot{\varphi}_1 - \dot{\varphi}_2)t + c) \tag{4}$$

When substituting $\dot{\varphi}_1 - \dot{\varphi}_2 = \psi$, with '$\psi$' a constant frequency, and neglecting the constant phase shift term 'c', equation 5 follows.

$$cos((\dot{\varphi}_1 - \dot{\varphi}_2)t + c) = cos(\psi t) \tag{5}$$

It thus follows, that theoretically for a pair of uncoupled bacterial rotators, $cos(\varphi_1 - \varphi_2)$ should translate to a plain harmonic wave. This suggests the measurement displayed in figure 18b to belong to a pair of cells with either no or minimal coupling. *E.coli* trapped in microcavities configured as shown in figure 18a behave as rotators with constant intrinsic frequencies, which show not to couple their motion to direct neighbouring cells.

Where there seems to be no coupled dynamic between two *E.coli* in separated cavities, two cells in cavities connected via microchannels, as depicted in figure 18c, show striking coupled behaviour. Cells exhibit periods of synchronization periodically interrupted by phase-slips. Figure 18d shows an exemplary instance illustrating the slow-fast periodic dynamics of $cos(\varphi_1 - \varphi_2)$ for pair of cells in connected cavities. The measurement shows cells periodically remain in-phase for $\sim10s$, while in anti-phase for just $\sim2s$, suggesting

cells to attract towards a synchronized state. The relation shown in equation 4 on this front no longer captures the coupled behaviour of two cells. As such, in the next section we introduce a different mathematical framework which has become integral to describing synchronization between biological oscillators.

7.2 Quantifying coupling between cells

The previous section presented an instance of coupled cell motion in a pair of cavities connected by microchannels. Its hypothesized that in the configuration of these channels lies the potential to control hydrodynamic interaction, and as such to mediate coupling between cells. To that extent, coupling is measured between many pairs of cells under a range of channel configurations, to afterwards extract the coupling strength by means of analytical modelling. This section elaborates on the process of quantifying coupled motion, thus drafting a guide to the engineered synchronization of single cells of *E.coli*.

7.2.1 The Adler model

The Adler model is a fundamental mathematical model that has been widely used to study synchronization in coupled systems. Originally proposed by Robert Adler in 1946 [42], this equation has been applied to a wide range of phenomena, from electrical circuits [61] to neuronal networks [62] and the pattern formation in populations of bacteria [63]. Its ability to extract coupling strength from observed behaviors makes it a valuable tool for understanding the mechanisms that underlie synchronization in a wide range of contexts. Here it is used to model the coupled behaviour between the cyclic motion of single cells.

Two *E.coli* trapped at opposing sides of a connected pair of cavities can be described as a set of $N = 2$ rotators, running around circular tracks, being fully specified in position by the phase angle their center of mass makes with the right side horizontal. Let φ_1 and φ_2 be the phases of the two cells, and assume that they rotate in clockwise direction with their respective natural frequencies ω_1 and ω_2, as shown in figure 19. Then the phase difference $\phi = \varphi_1 - \varphi_2$ between the two cells evolves according to a first-order differential equation of the form: $\dot{\phi} = f(\phi)$.
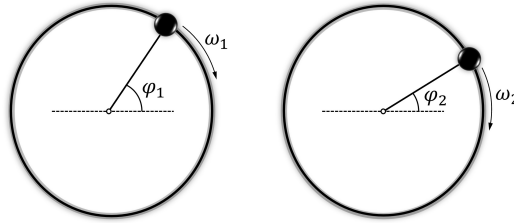

Figure 19: Schematic model of a pair of cells in connected cavities, described by particles running around circular tracks. The black spherical particles represent each cell's center of mass, with ω_1 and ω_2 their respective natural frequencies and the phase angles φ_1 and φ_2 which are measured with respect to the right horizontal.

The phase difference between cells can be characterized as a periodic function $f(\phi) = f(\phi + 2\pi)$, which can be expressed by its Fourier expansion $f(\phi) = a_0 + \sum_{n=1}^{\infty} a_n cos(n\phi) +$

$b_n sin(n\phi)$. To capture only the essential synchronization dynamics the model is further simplified to include only first order harmonics, therefore assuming $f(\phi) = a_0 + a_1 cos(\phi) + b_1 sin(\phi)$. The resulting model for describing phase synchronization between cells is finally reformulated as the Adler equation shown in equation 6.

$$\dot{\phi} = \Delta\omega - ksin(\phi - \phi_0) \tag{6}$$

Here $\Delta\omega = a_0$ represents the frequency mismatch $\omega_1 - \omega_2$ between cells, $k = \sqrt{a_1^2 + b_1^2}$ the coupling strength and $\phi_0 = atan(-a_1/b_1)$ the phase delay of the hypothetical restoring force. Noteworthy is that phase-locking between cells ($\dot{\phi} = 0$) can only exist as a stable state for $\lim_{t\to\infty} (f(\phi))$, when the frequency mismatch is small enough relative to the coupling strength, or $|\Delta\omega| \leq k$ [43]. However, the periodic slow-fast dynamic behaviour of $cos(\varphi_1 - \varphi_2)$ that is observed more resembles the case where $|\Delta\omega| > k$.

7.2.2 Parameter estimation from empirical data

From the derived Adler equation (equation 6), it is clear that the dynamics of the phase difference ϕ is dependent on the frequency mismatch $\Delta\omega$, the coupling strength k and the phase delay ϕ_0. The phase delay ϕ_0 of the restoring force can be deduced from the notation that $min(\dot{\phi}) = \dot{\phi}|_{\phi=\phi_0+0.5\pi}$, meaning the absolute gradient in phase difference between a pair of interacting cells is lowest at $\phi(t) = \phi_0 + 0.5\pi$. Figure 20 shows the slow-fast periodic dynamics of the phase difference between a pair of oscillators from slightly different starting positions, with ϕ_0 set to -0.5π, and $|\Delta\omega| > k$. From observation in experiments it is known cells mostly exhibit slow phase difference dynamics when they are in-phase, suggesting $\phi_0 = -0.5\pi$ to be a good estimate in describing their coupled behaviour.
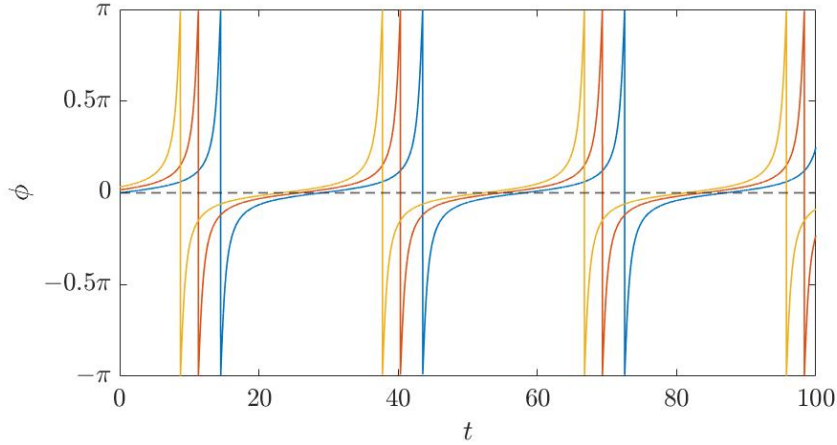

Figure 20: Evolution of the phase difference for a pair of interacting oscillators with $\phi_0 = -0.5\pi$ and $|\Delta\omega| > k$, from three slightly different starting positions around 0. The slow crossing through $\phi = \phi_0 + 0.5\pi$ indicated with the horizontal dotted line implies slow in-phase dynamics.

The oscillation period of the phase difference can be derived by means of separation of variables, as shown below in equation 7.

$$T = \int dt = \int_0^{2\pi} \frac{d\phi}{\Delta\omega - k sin(\phi - \phi_0)} = \frac{2\pi}{\sqrt{\Delta\omega^2 - k^2}} \tag{7}$$

The periodicity of the slow-fast dynamic of $f(\phi)$ is governed by the relation between the frequency mismatch $\Delta\omega$ and the coupling strength k. This oscillation period is unique for every pair of cells, and can be estimated directly from the measured data by means of the fast Fourier transform (FFT). We apply a local least-squares smoothing function based on polynomial approximation, originally proposed by Savitsky and Golay [64], and find the location of the smoothed magnitude peak. For the measurement displayed in figure 18b, we find 0.073Hz as a frequency estimate for the slow-fast periodicity, translating to an oscillation period T of $13.7s$.

Upon estimation of the oscillation period T, we remain with two variables ($\Delta\omega$ and k) which must comply with equation 7. Thus, we may fully determine the dynamics of $\dot{\phi} = f(\phi)$ by finding the best fit for the coupling strength k to the data. It is worth noting that typically with $T < 60s$, the dynamics of $\dot{\phi} = f(\phi)$ is most sensitive for change in k in the range $0 < k < 1$, deciding the gradient between the slow-fast dynamics. While for variation in k in the range $k > 5$ the dynamics remain nearly unaffected. As such, we numerically solve the Adler equation (eq 6) for the range of coupling strengths shown in eq 8.

$$k = \{0.01x | x \in [0, 0.49]\}, \{0.025y | y \in [0.5, 1]\}, \{0.05z | z \in [1.05, 5]\} \tag{8}$$

By means of computing the summed error (SE) of the squared residual, the relative 'goodness' of a fit can be determined for a certain value of k. Here the residual represents the vertical distance between the fit and the data, which is computed and summed over all discrete n sampling points in the data, see equation 9 below.

$$SE = \sum_{i=1}^{n} r_i^2 = \sum_{i=1}^{n} (y_i - \hat{y}_i)^2 \tag{9}$$

After numerically solving $\dot{\phi} = f(\phi)$ for a certain k, we horizontally translate the Adler function over the data by discrete steps of $dt = \{0.2t | t \in [0, T]\}$ in order to find the best overlap (with minimal SE). In this way, we find the combination of dt and k which locate the global minimum of the summed square residual. Figure 21 shows two cross-sections of the objective (SE) surface both intersecting through the global minimum, one orthogonal to the k axis (left panel) and the other to the dt axis (right panel). For the measurement shown in figure 18b, $k = 0.41$ leads to minimum fitting error of the discussed Adler model to the experimental data.
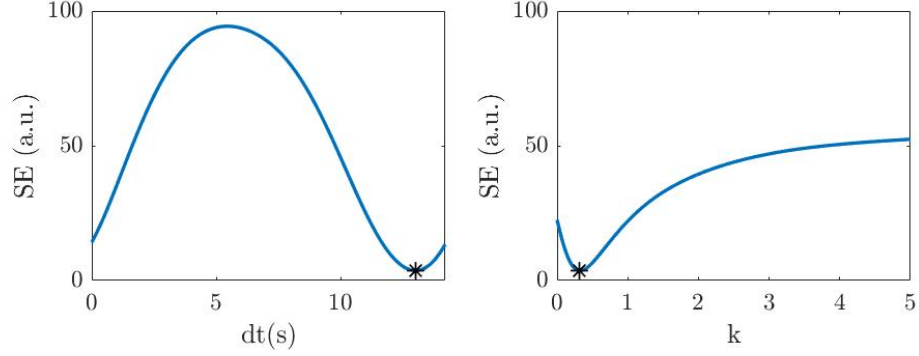
Figure 21: Two views of the global minimum summed squared error located at $k = 0.41$ (annotated with a black marker) of the Adler model fitted to the experimental data displayed in figure 18d. (Left panel) $SE - dt$ plane through the global minimum. (Right panel) $SE - k$ plane through the global minimum.

Finally we show that following the method of parameter estimation laid out above, for the measurement in figure 18b, the discussed Adler model (equation 6) fits the data as summarized in figure 22. Figure 22a shows how the fits are translated over the data to find the best overlap (for every numerically solved Adler function with discussed range in k as shown in eq 8). Figure 22b shows how the variation in k characterizes the Adler function.
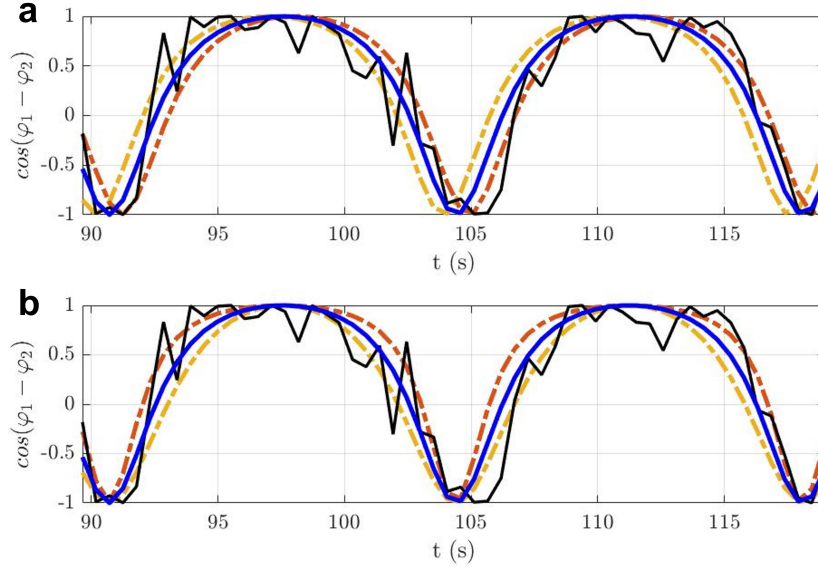
Figure 22: Process of k-estimation for the measurement shown in black. (a) Three fits with k fixed at 0.41 and varying dt. The best fit is shown in blue, with fits off by -0.5s (yellow line) and +0.5s (orange line). (b) Three fits with the best fit at $k =0.41$ shown in blue, and fits at $k =0.26$ (yellow) and $k =0.65$ (orange).

34

8 Extended data

8.1 Continued trapping

In this supplement we present a measurement of cell motion of a trapped *E.coli* cell inside an $8\mu m$ circular microcavity, see figure 23. Trapping was sustained for over 13min, during which the bacterium was observed to traverse the cavity, performing clockwise rotations. Tracking was performed as outlined in section 6.4.1. This experiment shows trapped *E.coli* not to tumble, but instead to swim continuously in predictable smooth clockwise circles with near constant speed.
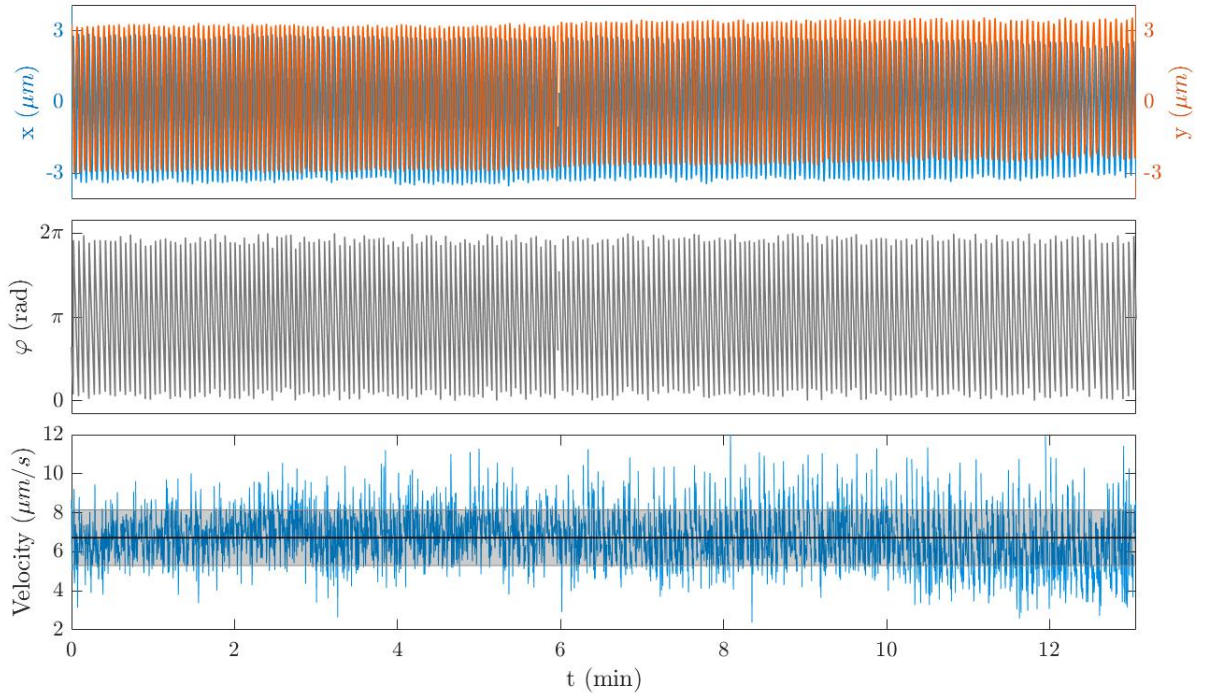
Figure 23: measurement of cell motion (relative to the cavity center) inside an $8\mu m$ microcavity. The upper panel shows the x and y coordinates of the cell center over time, the middle panel displays cell phase angle, and the lower panel cell velocity. The lower panel highlights the mean speed (black line) and the standard deviation (grey shade).

8.2   Extended measurements of trapping in large cavities

In figure 24 we present supplementary measurements of trajectories of *E.coli* trapped in large cavities (defined as cavities more than twice the size of the cell including flagella), where cells were observed to alternate between swimming at the cavity wall and in the cavity interior. Cells became temporarily trapped at the cavity wall, during which they would be guided by the boundary to traverse the cavity in clockwise direction. When cells would escape the wall they were observed to swim over the cavity floor with clockwise circular trajectories.

a Single cell trajectory in a 25μm cavity, presented as well in the main text (fig 2a right panel)

b Single cell trajectory in a 25μm cavity, extended data to figure 2b (right panel)

c Single cell trajectory in a 30μm cavity
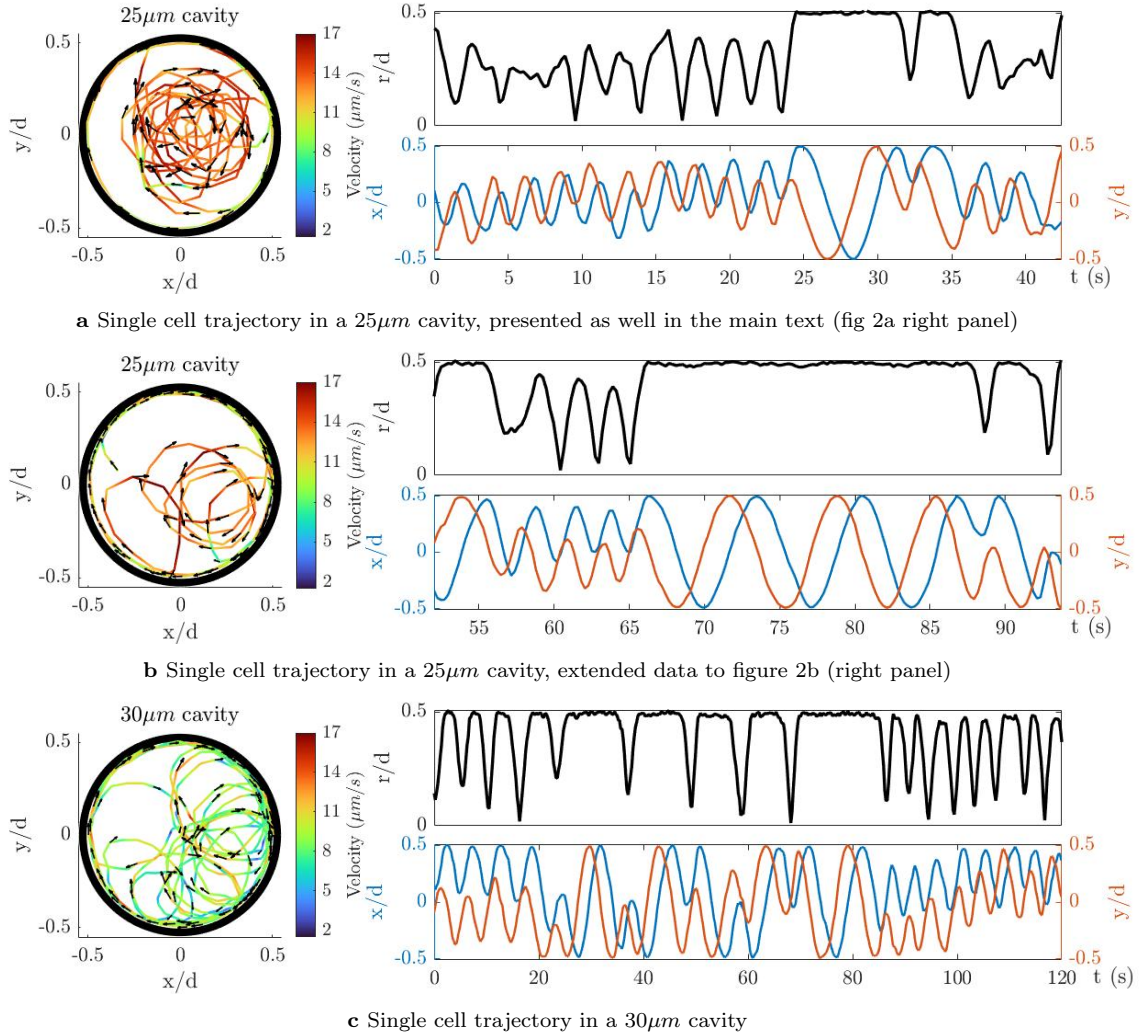
Figure 24: Three cell trajectories of trapped *E.coli* in large cavities. For each trajectory the velocity maps are displayed in the left panel. Swimming velocity is indicated by color, and arrows indicate the swimming direction. The time traces of the normalized distance of cells to the cavity center, as well as cell x-y coordinates, are shown in the upper right and lower right panels respectively. Shown graphs are supplementary to figure 2a (right panel) in the main text. Tracking was performed manually with ImageJ software.

8.3 Surface swimming

In this supplementary section, we present an exemplary measurement of the typical free surface swimming behavior of *E.coli* that we observed. We observed that cells swam in clockwise circular trajectories over the free PDMS surface, as shown in figure 25. The experiment was conducted following the procedure outlined in section 6.3, and cells were measured on a section of the substrate outside the cavity array.

a Microscopic image of cells swimming over a flat PDMS surface

b Cell trajectories. Arrows indicating cell swimming direction were added manually
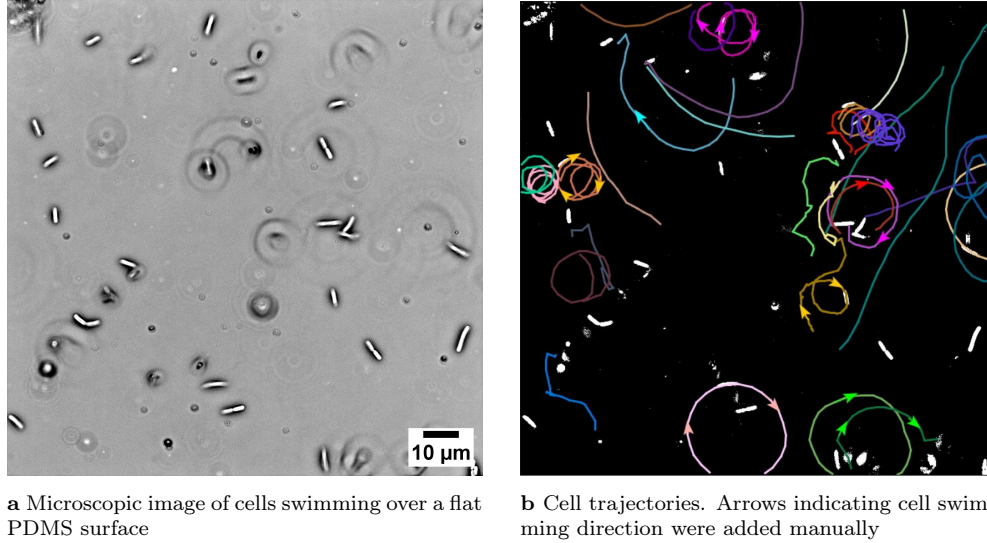
Figure 25: Measurement of cell motion over a flat surface. Tracking was performed with the TrackMate toolbox of ImageJ.

8.4 Data fitting - slow-fast dynamics

In this supplementary page, we present additional fits of the Adler model (see section 7.2.1) to the data. The observed behavior of the cells is well described by the slow-fast regime of the Adler function (eq 6), where $k < |\Delta\omega|$, as has been elaborated in section 7.2.2. Figure 26a shows the resulting fit to the measurement presented in the main text (see figure 4a), where cells were observed to periodically remain in-phase for up to $\sim 16s$, alternated by fast phase-slips of $\sim 5s$. The phase difference between cells exhibited 2π periodicity, as shown in figure 4b, where the same cell consistently overtook the other upon accumulating a phase offset. Note that the fit displayed in figure 4b was not computed separately, but is rather the unwrapped version of the fitted function displayed in figure 4a.
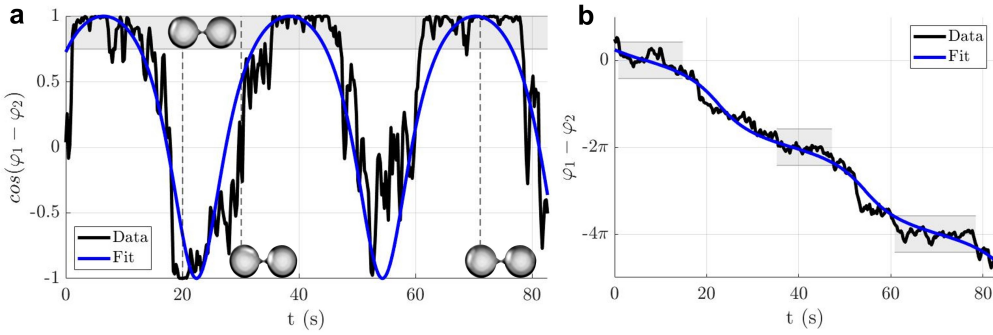
Figure 26: Slow-fast dynamics of the phase difference between a pair of cells in connected cavities, with cavity diameters of $8\mu m$ and channel length and width both measuring $0.5\mu m$. (a) Measured phase difference of two cells in coupled cavities (in black), fitted with the Adler model (in blue). Insets show the frame in the recording corresponding to the time point in the diagram. The synchronized state is highlighted with a gray shade. (b) Unwrapped phase difference shows a 2π periodic staircase-like trend. The grey shade correspond to the time cells were in the synchronized state, as indicated in sub figure a.

Our research involved the observation of the phase difference dynamics of cells and how it is influenced by channel geometry. As such, we further investigated how the phase dynamics is modulated by estimating the coupling strength, which was discussed in section 7.2.2. Extended fits to measurements in $7\mu m$ diameter cavities with channel widths $0.5\text{-}0.9\mu m$ and channel lengths $0.5\text{-}2\mu m$ are shown in figure 27a-e.
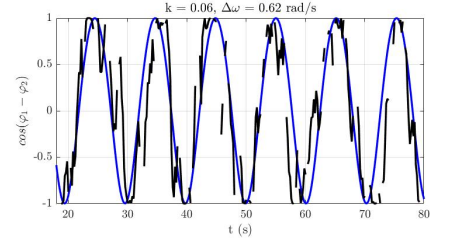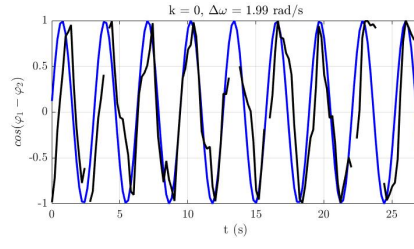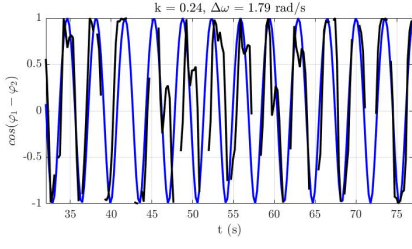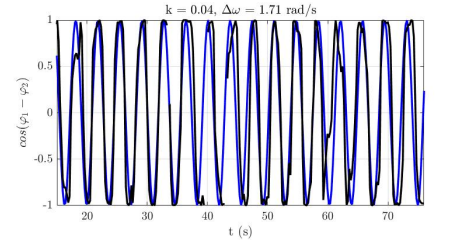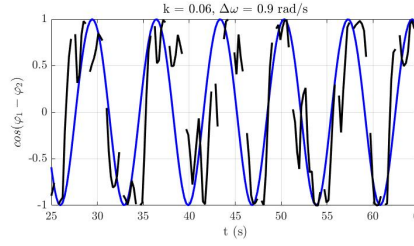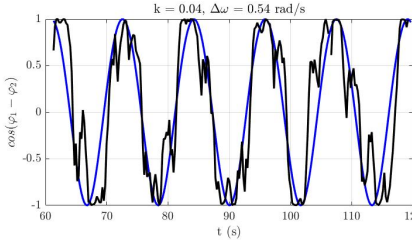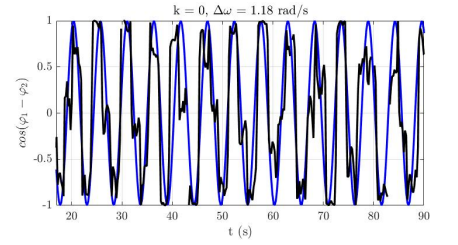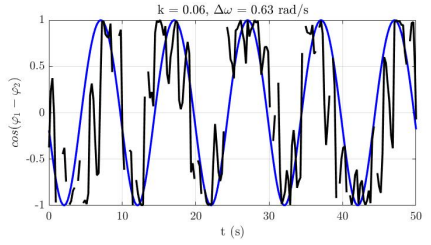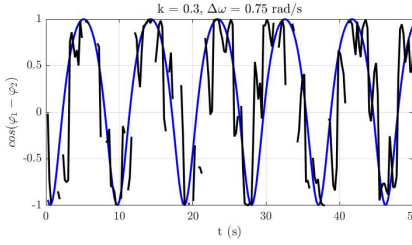
a Channel width $0.5\mu m$, channel length $0.5\mu m$
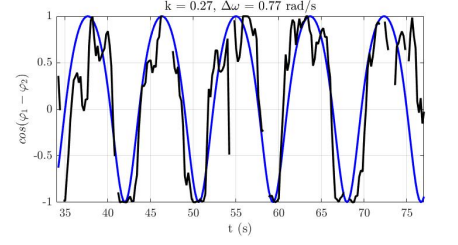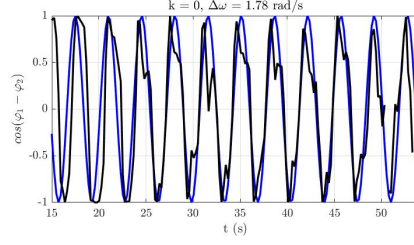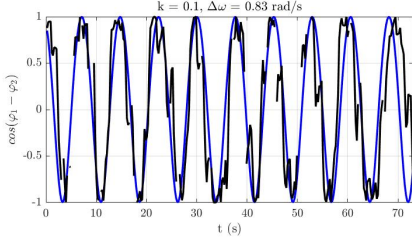
b Channel width $0.7\mu m$, channel length $0.5\mu m$
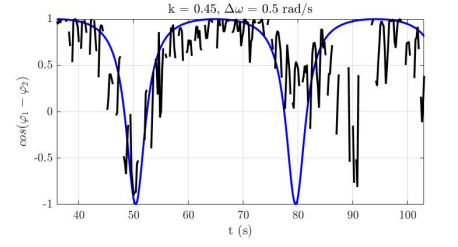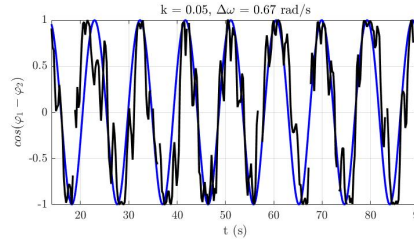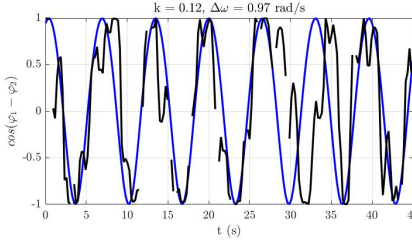
c Channel width $0.9\mu m$, channel length $0.5\mu m$

d Channel width $0.9\mu m$, channel length $1\mu m$

e Channel width $0.9\mu m$, channel length $2\mu m$

Figure 27: Extended fits to figures 3e-f in the main text. Panels show fits of the Adler model (in blue) to measurements of phase difference between cells (in black) in connected $7\mu m$ cavities.

8.5   Supplementary tables to figures

This supplementary section presents accompanying tables to figure 2c and figures 3e-f in the main text.

Well diameter	#Measurements	Mean $\pm$ std ($\mu m/s$)
$5\mu m$	154	4.7 ± 1.7
$6\mu m$	217	5.1 ± 2.1
$7\mu m$	226	5.6 ± 2.2
$8\mu m$	291	6.5 ± 2.6
$9\mu m$	46	7.6 ± 2.6
$14\mu m$	104	9.7 ± 3.3
$19\mu m$	125	10 ± 3.5
$25\mu m$	100	10 ± 3.3
$30\mu m$	83	9.5 ± 3.7
Surface	304	13 ± 4.7

Table 3: Measured cell velocities in different sized confinements compared to that on a surface. Table presents accompanying data to figure 2c in the main text.

$d - c_l - c_w$ (μm)	#Measurements	k (mean $\pm$ std)
7-0.5-0.5	35	0.06 ± 0.11
7-0.5-0.7	25	0.11 ± 0.11
7-0.5-0.9	11	0.14 ± 0.14
7-1-0.9	24	0.07 ± 0.10
7-2-0.9	15	0.10 ± 0.13

Table 4: Measured coupling strengths between cells oscillating in opposite sides of connected pairs of microcavities. Table presents accompanying data to figures 3e-f in the main text.

8.6 Additional coupling dynamics

8.6.1 In-phase and anti-phase synchronization

Additionally to the periodic slow (in-phase) - fast (out-of-phase) phase difference dynamics discussed in the main text, we observed instances of both slow dynamics in-phase and in anti-phase, periodically alternated by fast phase-slips, which is not captured by the Adler model derived in section 7.2.1. Two of these measurements are shown in figure 28, where the phase difference diagram resembles a trapezoidal waveform with occasional shoulders on the diagonal, indicating perturbations where one of the cells swam into the channel opening and momentarily stopped. We note these shoulders to occur approximately once every phase-slip, translating to perturbation frequencies of $\sim$0.2Hz and $\sim$0.4Hz for the measurements shown in figures 28a and 28b respectively. Interestingly, the periods cells were observed to remain in-phase and in anti-phase in both measurements ($\sim$5s in fig 28a and $\sim$2.5s in fig 28b), corresponded with the time between to perturbations. Thus, alternatively to slow-fast-slow coupling, we speculate that the measurements below may be modelled assuming cells sustained both in-phase and anti-phase synchronization, but periodic phase-slips originated from strong cyclic perturbations to the system of oscillators.
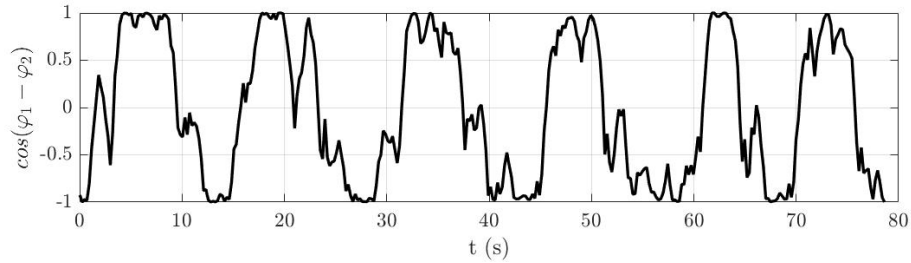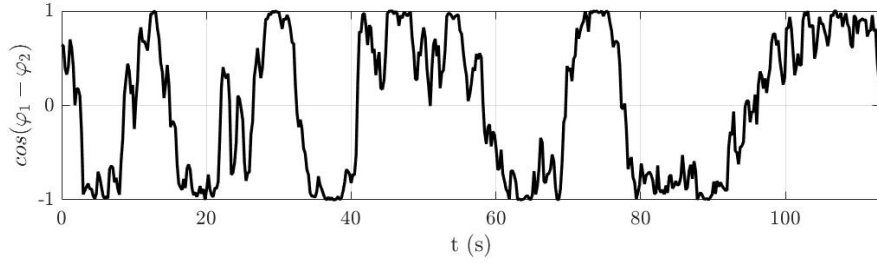

a Cavity diameter $7\mu m$, channel width $0.9\mu m$, channel length $1\mu m$
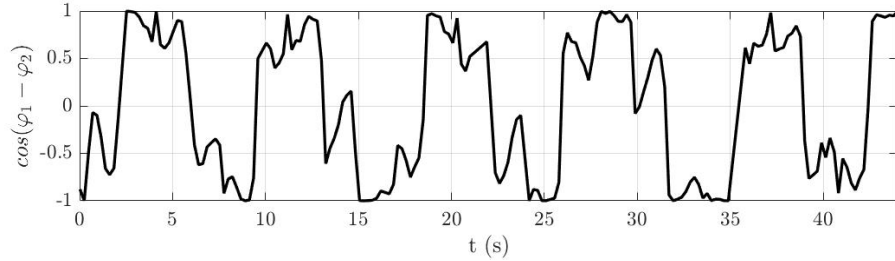
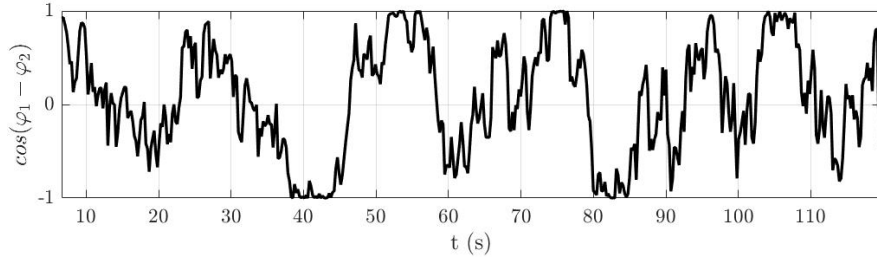**b** Cavity diameter $7\mu m$, channel width $0.9\mu m$, channel length $2\mu m$

Figure 28: Two measurements of *E.coli* cells swimming in connected microcavities showing alternating states of in-phase and anti-phase synchronization. Tracking was performed as outlined in section 6.4.1

Figure 29 presents two measurements where cells were also observed to display both in-phase and anti-phase synchronization. However, cells were found to spend varying periods of time in each of the synchronized states, with the time spent in anti-phase ranging from 5 to 12 seconds, and the time spent in-phase ranging from 1 to 13 seconds (see fig 29a). We speculate that periodic perturbations and/or biological noise occasionally were strong enough to kick the system out of a sync state. As such, perturbation events where one of the cells bumps into the channel opening may be adequately modeled as events with a certain level of periodicity and random amplitude. Furthermore, the shown measurements indicate phase-slips would occur at times as either a fast or slow dynamic. It is likely that phase-slips were slowed down or disrupted by periodic perturbations or by other cells in the culture that abruptly entered and left. This latter phenomenon has been sporadically seen to occur in accompanying video recordings.

a Cavity diameter $7\mu m$, channel width $0.9\mu m$, channel length $2\mu m$
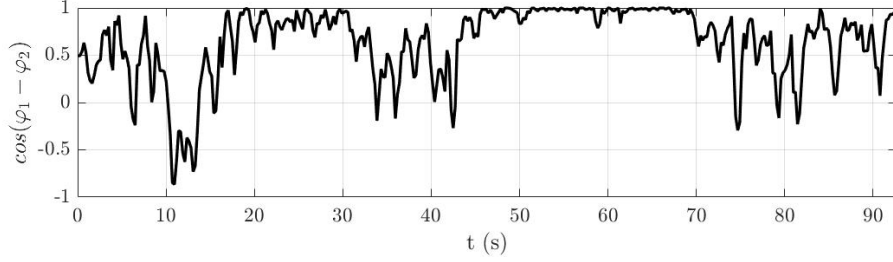

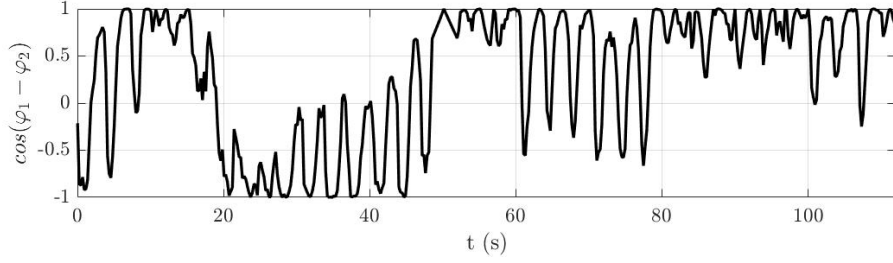**b** Cavity diameter $7\mu m$, channel width $0.7\mu m$, channel length $2\mu m$

Figure 29: Two measurements of *E.coli* cells swimming in connected microcavities which were observed to sustain in-phase and anti-phase synchronization for varying periods of time, as well as slow phase-slips additionally to fast phase-slips. Tracking was performed manually.

8.6.2 Continued in-phase synchronization

Next, in figure 30 we present two instances where cells in the synchronized state were observed to, upon accumulating a phase offset, resist a full phase slip. Instead the cells returned to the synchronized state, indicating the presence of a stable equilibrium state (in-phase sync) between oscillators. Besides, figure 30a displays in-phase synchronization between cells could be sustained for over 30 seconds. We assume the observed coupling dynamic may be described by the Adler model in the regime where $k > |\Delta\omega|$.

a Cavity diameter $7\mu m$, channel width $0.5\mu m$, channel length $0.5\mu m$

b Cavity diameter $7\mu m$, channel width $0.9\mu m$, channel length $1\mu m$

Figure 30: Two measurements of *E.coli* cells swimming in connected microcavities which were observed to sustain continued periods of in-phase synchronization. Tracking in (a) was performed manually, in (b) tracking was performed as outlined in section 6.4.1

8.7 Measurement on inverted cavities

In order to investigate the role of gravity in cell trapping, an experiment was conducted on inverted PDMS microcavities. Two substrates were prepared according to the methodology presented in section 6.1.3. One of the substrates was moulded on the pattern-free section of the silicon wafer, resulting in a flattened PDMS top layer. To create a sandwich-like configuration, a 35 μl aliquot of cell culture was dispensed on the plain substrate, on top of which subsequently the patterned substrate was placed. Figure 31 draws a comparison of the adjusted experiment setup (fig 31b), compared to previous experiments (fig 31a).
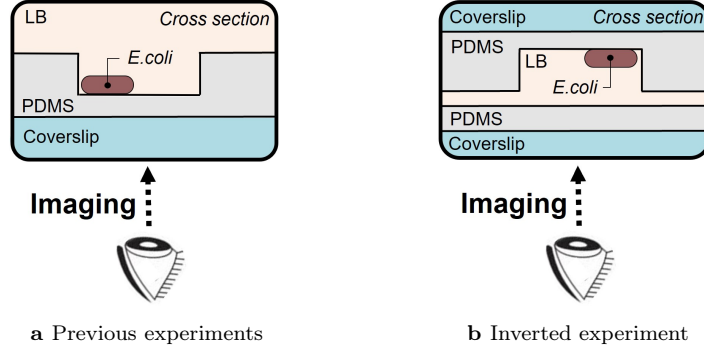

a Previous experiments   **b** Inverted experiment

Figure 31: Schematics of the experiment configurations.

Measurements were taken on inverted cavities $2.5\mu m$ deep and $30\mu m$ in diameter. We set the focal plane to the height corresponding to the cavity ceiling, and as such only measured cells that were swimming as depicted in figure 31b. Interestingly, trapped cells were observed to swim over the cavity ceiling (and along the cavity wall), as shown in figure 32, implying they swam upward against gravity to become trapped at the top surface. Moreover, we observed cells to both traverse cavities in clockwise (CW), as in counter-clockwise direction (CCW), while strictly inverting the CW motion from previous experiments (see fig 1b-c), would logically translate to CCW rotations in inverted cavities. We note the observation to contradict the right-handed behaviour of *E.coli* measured in other works [32], but regard the further quantitative analysis out of scope.
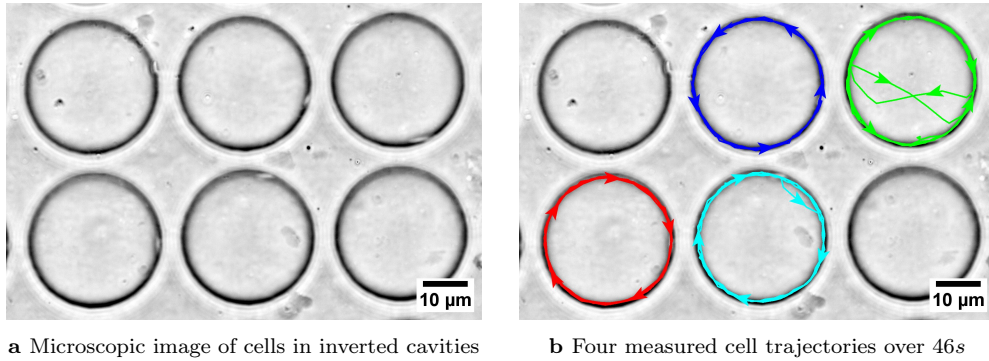

a Microscopic image of cells in inverted cavities   **b** Four measured cell trajectories over $46s$

Figure 32: Cell motion in inverted $30\mu m$ cavities (see fig 31b). Tracking was performed manually.

8.8 Additional configurations for cell trapping

In this supplementary, we present measurements of cell movement in various additional trapping configurations. The substrate used for the experiments was moulded on a patterned silicon wafer which was etched to 2.5 μm depth, and experiments were carried out according to the method outlined in section 6.3. Cell motion was among others measured in square circuits with $30\mu m$ long, $4\mu m$ wide microchannels, where some cells were observed to navigate the structure in clockwise direction (fig 33a-b left panel). In asymmetric doublets with a square and a circular side connected by a ($4\mu m$ wide) microchannel, cells became trapped in either side, performing clockwise rotations (fig 33a-b middle panel), similarly as in $6x9\mu m$ rectangular traps (fig 33a-b right panel). We note the established right-handedness of *E.coli* [32] to translate to clockwise rotations in various geometries, providing an outlook on the potential of open on-chip environments in the directional ordering of cells.
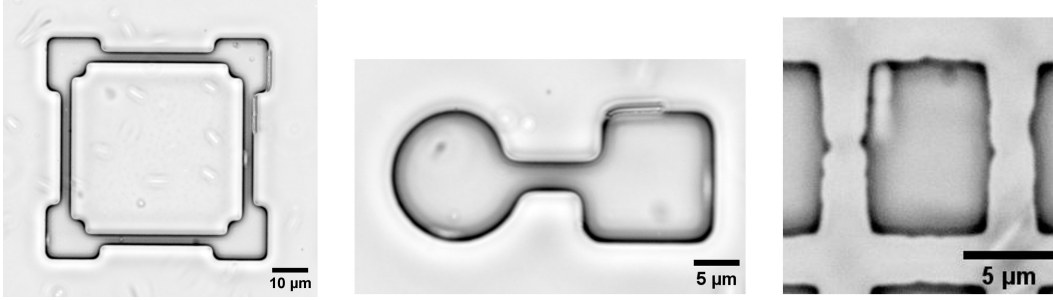
a Microscopic images of cells in various trap geometries
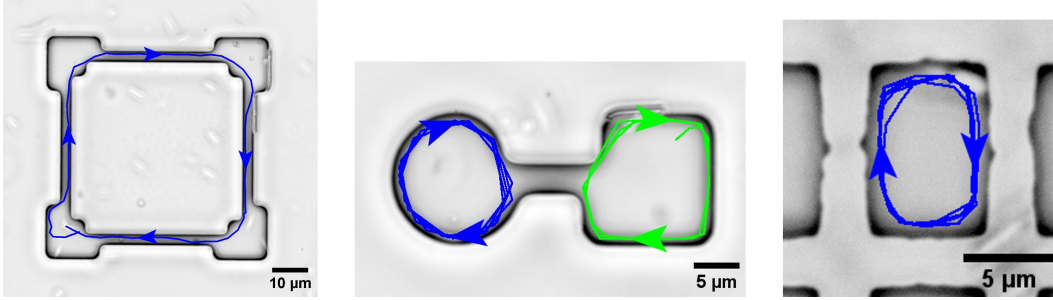
b Single cell trajectories measured in each of the configurations

Figure 33: Single measurements of cell movement in a square shaped circuit (left panels), asymmetric doublet (middle panels) and rectangular trap (right panels). Tracking was performed manually with the ImageJ toolbox.

References

[1] Lauga, E., Powers, T. "The hydrodynamics of swimming microorganisms". *Reports on Progress in Physics* (2009).

[2] Marken, W., Powers, W. "Random-Walk Chemotaxis: Trial and Error as a Control Process". *Behavioural Neuroscience* (1989).

[3] Chen, C., Liu, S., Shi, X. et al. "Weak synchronization and large-scale collective oscillation in dense bacterial suspensions". *Nature* (2017).

[4] Rosłoń, I., Japaridze, A., Steeneken, P. et al. "Probing nanomotion of single bacteria with graphene drums". *Nature Nanotechnology* (2022).

[5] Romera, M., Talatchian, P., Tsunegi, S. et al. "Vowel recognition with four coupled spin-torque nano-oscillators". *Nature* (2018).

[6] Rubenstein, M., Cornejo, A., Nagpal, R. "Programmable self-assembly in a thousand-robot swarm". *Science* (2014).

[7] Miyata, M., Robinson, R., et al. "Tree of motility – A proposed history of motility systems in the tree of life". *Genes to Cells* (2020).

[8] Karmakar, R. "State of the art of bacterial chemotaxis". *Journal of Basic Microbiology* (2021).

[9] Toole, G., Kaplan, H., Kolter, R. "Biofilm formation as microbial development". *Annual Review of Microbiology* (2000).

[10] Allison, C., Coleman, N., et al. "Ability of Proteus mirabilis to invade human urothelial cells is coupled to motility and swarming differentiation". *Infection and Immunity* (1992).

[11] Piskovsky, V., Oliveira, N. "Bacterial motility governs the evolution of antibiotic resistance in spatially heterogeneous environments". *bioRxiv* (2022).

[12] Berg, H. *E. coli in Motion*. Springer New York, 2004.

[13] Molaei, M., Barry, M., Stocker, R. et al. "Failed escape: Solid surfaces prevent tumbling of Escherichia coli". *Physical Review Letters* (2014).

[14] Wioland, H., Goldstein, R. et al. "Ferromagnetic and antiferromagnetic order in bacterial vortex lattices". *Nature Physics* (2016).

[15] Wioland, H., Lushi, E., Goldstein, R. "Directed collective motion of bacteria under channel confinement". *New J. Phys.* (2016).

[16] Glass, L. "Synchronization and rhythmic processes in physiology". *Nature* (2001).

[17] De Bruin, G., Ypey, D., Van Meerwijk, M. "Synchronization in Chains of Pacemaker Cells by Phase Resetting Action Potential Effects". *Biological Cybernetics* (1983).

[18] Buzsáki, G., Logothetis, N., Singer, W. "Scaling Brain Size, Keeping Timing: Evolutionary Preservation of Brain Rhythms". *Neuron* (2013).

[19] Goldstein, R., Polin, M., Tuval, I. "Noise and Synchronization in Pairs of Beating Eukaryotic Flagella". *Physical Review Letters* (2009).

[20] Discher, D., Dong C., Fredberg, J. et al. "Biomechanics: Cell Research and Applications for the Next Decade". *Annals of biomedical engineering* (2009).

[21] Janmey, P., McCulloch, C. "Cell mechanics: Integrating cell responses to mechanical stimuli". *Annual Review of Biomedical Engineering* (2007).

[22] Guck, J., Schinkinger, S., Lincoln, B. et al. "Optical Deformability as an Inherent Cell Marker for Testing Malignant Transformation and Metastatic Competence". *Biophysical Journal* (2005).

[23] Kasas, S., Stupar, P., Dietler, G. "AFM contribution to unveil pro- and eukaryotic cell mechanical properties". *Seminars in cell developmental biology* (2018).

[24] Nagod, S., Halse, S. "Evolution of MEMS Technology". *International Research Journal of Engineering and Technology* (2017).

[25] Rettig, J., Folch, A. "Large-scale single-cell trapping and imaging using microwell arrays". *Analytical Chemistry* (2005).

[26] Pitruzzello, G., Thorpe, S., et al. "Multiparameter antibiotic resistance detection based on hydrodynamic trapping of individual E. coli". *Lab on a Chip* (2019).

[27] Wadhwa, N., Berg, H. "Bacterial motility: machinery and mechanisms". *Nature Reviews Microbiology* (2021).

[28] Qiu, T., Lee, T., Mark, A. et al. "Swimming by reciprocal motion at low Reynolds number". *Nature Communications* (2014).

[29] Frymier, P., Ford, R., Berg, H., et al. "Three-dimensional tracking of motile bacteria near a solid planar surface". *Proc. Natl Acad. Sci. USA* (1995).

[30] Lauga, E., DiLuzio, W., Whitesides, G. et al. "Swimming in circles: motion of bacteria near solid boundaries". *Biophysical journal* (2006).

[31] Liu, Z., Papadopoulos, K. "Unidirectional motility of Escherichia coli in restrictive capillaries". *Applied and Environmental Microbiology* (1995).

[32] DiLuzio, W., Turner, L., Mayer, M. et al. "Escherichia coli swim on the right-hand side". *Nature* (2005).

[33] Vigeant, M., Ford, R., et al. "Reversible and Irreversible Adhesion of Motile Escherichia coli Cells Analyzed by Total Internal Reflection Aqueous Fluorescence Microscopy". *Applied and Environmental Microbiology* (2002).

[34] Sipos, O., Nagy, k., et al. "Hydrodynamic Trapping of Swimming Bacteria by Convex Walls". *Physical Review Letters* (2015).

[35] Galajda, P., Keymer, J., et al. "A Wall of Funnels Concentrates Swimming Bacteria". *Journal of Bacteriology* (2007).

[36] Di Leonardo, R., Angelani, L., et al. "Bacterial ratchet motors". *Proceedings of the National Academy of Sciences* (2010).

[37] Tokárováa, V., Perumala, A. et al. "Patterns of bacterial motility in microfluidics-confining environments". *Proceedings of the National Academy of Sciences* (2021).

[38] Wioland, H., Goldstein, R. et al. "Confinement Stabilizes a Bacterial Suspension into a Spiral Vortex". *Physical Review Letters* (2013).

[39] Beppu, K., Izri, Z. et al. "Geometry-driven collective ordering of bacterial vortices". *Soft Matter* (2017).

[40] Liu, J., Prindle, A. et al. "Metabolic co-dependence gives rise to collective oscillations within biofilms". *Nature* (2015).

[41] Golestanian, R., Yeomans, J., Uchida, N. "Hydrodynamic synchronization at low Reynolds number". *Soft Matter* (2011).

[42] Adler, R. "A Study of Locking Phenomena in Oscillators". *Proceedings of the IRE* (1946).

[43] Strogatz, S., Mirollo, R. "Collective synchronisation in lattices of nonlinear oscillators with randomness". *J. Phys. A: Math. Gen. 21 L699* (1988).

[44] Willms, A., Kitanov, P., Langford, W. "Huygens' clocks revisited". *Royal Society Open Science* (2017).

[45] Vicsek, T., Zafeiris, A. "Collective motion". *Physics Reports* (2012).

[46] Strogatz, S., Steward, I. "Coupled Oscillators and Biological Synchronization". *Scientific American* (1993).

[47] Néda, Z., Ravasz, E. et al. "The sound of many hands clapping". *Nature* (2000).

[48] Uchida, N., Golestanian, R. "Synchronization and Collective Dynamics in a Carpet of Microfluidic Rotors". *Physical Review Letters* (2010).

[49] Rosłoń, I., Japaridze, A. "Microwell-enhanced optical detection of single bacteria". *bioRxiv* (2023).

[50] Rangelow, I.) "Critical tasks in high aspect ratio silicon dry etching for microelectromechanical systems". *Journal of Vacuum Science Technology A 21* (2003).

[51] DePalma. V., Tillman, N. "Friction and Wear of Self -Assembled Trichlorosilane Monolayer Films on Silicon". *Langmuir* (1989).

[52] Raj, K., Chakraborty, S.) "PDMS microfluidics: A mini review". *Journal of Applied Polymer Science* (2020).

[53] Kim, G., Lee, S., Kim, C. "Assessment of the Physical, Mechanical, and Tribological Properties of PDMS Thin Films Based on Different Curing Conditions". *Materials* (2021).

[54] Tan, S., Nguyen, N., Chua, Y., et al. "Oxygen plasma treatment for reducing hydrophobicity of a sealed polydimethylsiloxane microchannel". *Biomicrofluidics 4* (2010).

[55] Merouane, A., Rey-Villamizar, N. et al. "Automated profiling of individual cell-cell interactions from high-throughput time-lapse imaging microscopy in nanowell grids (TIMING)". *Bioinformatics* (2015).

[56] Xie, J., Khan, S., Shah, M. "Automatic tracking of escherichia coli in phase-contrast microscopy video". *IEEE Transactions on Biomedical Engineering* (2009).

[57] Van Valen, D., Kudo, T., Lane, K. et al. "Deep Learning Automates the Quantitative Analysis of Individual Cells in Live-Cell Imaging Experiments". *PLoS computational biology* (2016).

[58] Lugagne, J., Lin, H., Dunlop, M. "DeLTA: Automated cell segmentation, tracking, and lineage reconstruction using deep learning". *PLoS computational biology* (2020).

[59] Yuen, H., Princen, J. et al. "Comparative study of Hough Transform methods for circle finding". *Image and Vision Computing* (1990).

[60] Pantaleone, J. "Synchronization of metronomes". *American Journal of Physics* (2002).

[61] Bhansali, P., Roychowdhury, J. "Gen-Adler: the Generalized Adler's equation for injection locking analysis in oscillators". *ASP-DAC '09: Asia and South Pacific Design Automation Conference* (2009).

[62] Oliaei, O. "Synchronization and phase synthesis using PLL neural networks". *IEEE International Symposium on Circuits and Systems* (2006).

[63] Liebchen, B., Cates, M., Marenduzzoa, D. "Pattern formation in chemically interacting active rotors with self-propulsion". *Soft Matter* (2016).

[64] Savitzky, A., Golay, M. "Smoothing and Differentiation of Data by Simplified Least Squares Procedures". *Analytical Chemistry* (1964).